Bhlhe40 Governs T Cell Effector Differentiation with Distinct Requirements in CD4 and CD8 T Cells for Anti-PD-1 and Anti-CTLA-4 Efficacy

Akata Saha[1*], Tomoyuki Minowa[1*], Alexander S. Shavkunov[1], Avery J. Salmon[1], Sunita Keshari[1], Suresh Satpati[2], Nicholas N. Jarjour[3†], Abhinav K. Jain[4], Kunal Rai[2], Kristen E. Pauken[1], Kenneth H. Hu[1,5], Brian T. Edelson[3], Ken Chen[6], Matthew M. Gubin[1#]

1. Department of Immunology, The University of Texas MD Anderson Cancer Center, Houston, TX, USA

2. Department of Genomic Medicine, The University of Texas MD Anderson Cancer Center, Houston, TX, USA

3. Department of Pathology and Immunology, Washington University School of Medicine, St. Louis, MO, USA

4. Department of Epigenetics and Molecular Carcinogenesis, The University of Texas MD Anderson Cancer Center, Houston, TX, USA.

5. James P. Allison Institute, The University of Texas MD Anderson Cancer Center, Houston, TX, USA

6. Department of Bioinformatics and Computational Biology, The University of Texas MD Anderson Cancer Center, Houston, TX, USA

[*] These authors contributed equally

[†] Current address: Versiti Blood Research Institute, Milwaukee, WI and Department of Biochemistry, Medical College of Wisconsin, Milwaukee, WI, USA

K.R. reports equity in Jivanu Therapeutics and Koshika Therapeutics, research funding from Cyclacel, and a consulting fee from Daiichi Sankyo that is unrelated to the current work. K.E.P. reports a patent on T cell exhaustion state-specific gene expression regulators and uses thereof (US2021/0309965 A1) that is unrelated to the current work. M.M.G. reports a personal honorarium from Springer Nature Ltd for his role as a Deputy Editor for the journal Nature Precision Oncology and serves as a paid consultant for Merck. No disclosures were reported by the other authors.

#Corresponding author:

Matthew M. Gubin, PhD
Department of Immunology
The University of Texas MD Anderson Cancer Center
7455 Fannin St., Unit 901
Houston, TX 77054
Phone (713) 745-9790
Email mgubin@mdanderson.org

ABSTRACT:

The transcriptional programs enabling T cells to mediate anti-tumor immunity remain incompletely defined. Here, we identify Bhlhe40 as a key transcriptional regulator that coordinates both CD4 and CD8 T cell effector programs, revealing divergent cell-specific requirements during anti-PD-1 versus anti-CTLA-4 immune checkpoint therapy (ICT). Using conditional knockout mice, we show that anti-PD-1 efficacy depends on CD8 T cell-intrinsic Bhlhe40, whereas anti-CTLA-4 remains effective through Bhlhe40-dependent CD4 T cell Th1 programs that buffer impaired effector function in Bhlhe40-deficient CD8 T cells. Mechanistically, loss of Bhlhe40 reduces IFN-γ production and skews CD8 T cells toward TCF-1-expressing progenitor exhausted/stem-like states at the expense of effector differentiation, impairing glycolytic fitness under both therapies and mitochondrial function during anti-PD-1 treatment, thereby revealing a Bhlhe40-dependent coupling between effector differentiation, cytokine production, and metabolic fitness that is particularly critical for anti-PD-1 efficacy. CD8 T cell-intrinsic Bhlhe40 also promotes critical ICT-induced remodeling from M2-like CX3CR1□ macrophages to inflammatory iNOS□ macrophages. Analysis of human cancer datasets supported our preclinical observations, revealing that *BHLHE40* is enriched in tumor-reactive and activated/exhausted CD8 T cells, where its expression is inversely correlated with *TCF7* (TCF-1) and positively associated with *TOX*, *GZMB*, and *IFNG*. Moreover, persistent CD8 T cell clones from basal cell carcinoma responders exhibited significantly higher *BHLHE40* expression at pre-treatment than those from non-responders to PD-1 blockade. Together, these findings establish Bhlhe40 not only as a transcriptional coordinator of T cell effector programs, but also as a therapy-specific, subset-dependent determinant that differentially governs CD4 and CD8 T cell contributions to anti-PD-1 and anti-CTLA-4 efficacy.

INTRODUCTION:

Immune checkpoint therapy (ICT) targeting PD-1 or CTLA-4 can elicit durable tumor regression in some patients, but many fail to respond[1-7]. While tumor-reactive T cells are central to ICT efficacy[8-16], the transcriptional programs that enable CD4 and CD8 T cells to mediate effective anti-tumor immunity remain incompletely defined[17-19]. Understanding these requirements is important because anti-PD-1 and anti-CTLA-4 each act through both overlapping as well as distinct mechanisms[20,21]. Basic helix-loop-helix family member e40 (Bhlhe40) has emerged as a critical transcription factor regulating immune responses[22]. Bhlhe40 often functions as a transcriptional repressor, which in some contexts involves binding promoter or enhancer regions of target loci[22-24]; however, it can also function as a transcriptional activator, particularly in cooperation with other transcription factors[25]. Bhlhe40 has also been shown to indirectly enhance gene transcription by sustaining intracellular acetyl-CoA to support histone acetylation[26]. Bhlhe40 is expressed across multiple cell types[27,28], including T cells, where its expression is driven by TCR engagement and CD28 co-stimulation, can be induced by inflammatory cytokines such as GM-CSF and IL-1β, and is restrained by PD-1 signaling[22,26,29,30]. Mice lacking Bhlhe40 in both CD4 and CD8 T cells are resistant to experimental autoimmune encephalomyelitis, reflecting the requirement for Bhlhe40 to repress IL-10 and promote GM-CSF production in T cells[23,27,31]. Conversely, these mice exhibit increased susceptibility to certain infections[24,32].

We recently demonstrated neoantigen (NeoAg)-specific intratumoral CD4 and CD8 T cells upregulate Bhlhe40 in tumor-bearing mice treated with anti-PD-1 or anti-CTLA-4 ICT[30]. Using CD4-Cre Bhlhe40$^{fl/fl}$ mice—where deletion occurs in both CD4 and CD8 T cells—we found that T cell-intrinsic Bhlhe40 is essential for tumor rejection in response to either ICT. Global deletion of Bhlhe40 disrupted T cell effector gene expression and impaired ICT-driven remodeling of the

tumor microenvironment (TME). Independent work demonstrated Bhlhe40 is required for response to anti-PD-1/PD-L1 ICT in preclinical models, with loss of T cell-intrinsic Bhlhe40 linked to defective mitochondrial fitness[26]. Thus, a central unresolved question is whether Bhlhe40 functions as a shared transcriptional node across immunotherapies or instead plays distinct, T cell-subset-specific roles that differentially govern responses to anti-PD-1 versus anti-CTLA-4, and through what mechanisms these effects are mediated.

Here, we dissect the cell-type-specific requirements for Bhlhe40 in ICT by selectively deleting it in CD8 T cells or in both CD4 and CD8 T cells using tumor models where both subsets are essential for therapeutic response. We show that CD8 T cell-intrinsic Bhlhe40 is required for tumor control by anti-PD-1, with additional contributions from CD4 T cell-intrinsic Bhlhe40, whereas anti-CTLA-4 efficacy is largely dependent on CD4 T cell-intrinsic Bhlhe40 and remains intact when Bhlhe40 is absent from CD8 T cells. Loss of Bhlhe40 skews CD8 T cells toward a more naïve or progenitor exhausted-like state and reduced acquisition of terminal effector features, particularly in the absence of ICT. In addition, Bhlhe40 supports glycolysis under both anti-PD-1 and anti-CTLA-4 therapies, sustains mitochondrial respiration primarily during anti-PD-1, and is essential for full ICT-induced myeloid remodeling from CX3CR1□ to iNOS□ macrophages. Analysis of multiple human cancer datasets demonstrates that *BHLHE40* is enriched in tumor-reactive and activated/exhausted CD8 T cell populations across tumor types, inversely correlated with *TCF7*, and positively associated with *TOX*, *GZMB*, and *IFNG*. Moreover, persistent CD8 T cell clones from basal cell carcinoma responders exhibited higher *BHLHE40* expression at pre-treatment than those from non-responders to PD-1 blockade. Our findings establish Bhlhe40 as a key regulator of T cell effector programming and as a transcriptional determinant of subset-specific functions that underlie response to anti-PD-1 versus anti-CTLA-4 therapy.

RESULTS:

Human Tumor-Reactive CD4 and CD8 Effector T Cells Express Bhlhe40

We previously found that Bhlhe40 is expressed in intratumoral CD4 and CD8 T cells and mice lacking Bhlhe40 in both CD4 and CD8 T cells fail to respond to anti-PD-1 or anti-CTLA-4 immune checkpoint therapy (ICT)[30]. To extend these findings to human tumors, we first examined *BHLHE40* expression across immune cell types inferred from The Cancer Genome Atlas (TCGA) RNA-sequencing (RNA-seq) data. Both CD4 and CD8 T cells consistently expressed *BHLHE40* across multiple cancer types (**Fig. 1A**). We next asked whether its expression is selectively enriched within human tumor-reactive CD8 T cells, since tumors can contain both tumor-specific CD8 T cells as well as non-tumor-reactive bystander CD8 T cells[33]. Tumor-reactive CD8 T cells were identified in studies by Oliveira et al. and Minowa et al.[34,35], which analyzed human cutaneous melanoma (an immunogenic tumor type that frequently responds to ICT), and acral melanoma (a less immunogenic tumor type), respectively. Reanalysis of datasets from both these studies revealed enrichment of *BHLHE40* in tumor-reactive CD8 T cells compared with predominately non-tumor-reactive CD8 T cells (**Fig. 1B**). Overall, these findings align with our observations in murine models, where Bhlhe40 is highly expressed within tumor-reactive populations[30].

CD8 T Cell-Intrinsic Bhlhe40 Is Essential for Anti-PD-1 but Not Anti-CTLA-4 Efficacy

We previously reported that *CD4-Cre Bhlhe40*$^{fl/fl}$ ($B^{\Delta T}$) conditional knockout (KO) mice lacking Bhlhe40 in both CD4 and CD8 T cells (because CD4-Cre is expressed in double-positive thymocytes[36]) fail to respond to anti-PD-1 or anti-CTLA-4 ICT[30]. Consequently, we first sought to determine whether Bhlhe40 expression specifically within CD8 T cells is required for the therapeutic efficacy of anti-PD-1 and anti-CTLA-4. We used *CD8 E8I-Cre* mice, in which Cre recombinase is driven by the E8I CD8 enhancer that is active exclusively in CD8 T cells[37]. We verified Bhlhe40 was specifically deleted in intratumoral CD8 T cells (and not CD4 T cells) in

isotype control antibody (Ab)-, anti-PD-1-, or anti-CTLA-4- treated *CD8 E8I-Cre Bhlhe40*$^{fl/fl}$ ($B^{\Delta CD8}$) mice bearing the 1956 MCA sarcoma tumor[30,38,39] (**Fig. S1A**). Using this well-characterized tumor model, we next injected 1956 tumor cells into Bhlhe40-sufficient *Bhlhe40*$^{fl/fl}$ ($B^{f/f}$) control mice, $B^{\Delta T}$ mice (Bhlhe40 KO in CD4 and CD8 T cells), $B^{\Delta CD8}$ mice (Bhlhe40 KO in CD8 T cells) and treated them with control Ab, anti-PD-1, or anti-CTLA-4 (**Fig. 2A**). Consistent with our prior findings[30], tumor outgrowth was observed in $B^{\Delta T}$ mice treated with anti-PD-1 or anti-CTLA-4 (**Fig. S1B**). While tumor regression occurred in anti-PD-1-treated $B^{f/f}$ control mice, anti-PD-1 failed to control tumor growth in $B^{\Delta CD8}$ mice (**Fig. 2B**). Interestingly, anti-CTLA-4 elicited effective tumor control in both $B^{f/f}$ and $B^{\Delta CD8}$ mice (**Fig. 2B**). We obtained similar results using the *Braf*^{V600E} *Pten*$^{-/-}$ *Cdkn2*$^{-/-}$ YUMM1.7[40]-modified Y1.7LI melanoma model[41] (**Figs. S1C and S1D**). To confirm that expression of Cre itself does not affect anti-tumor immune responses, we compared *CD8 E8I-Cre Bhlhe40*$^{+/+}$ mice to $B^{f/f}$ mice and observed comparable tumor growth and responses to ICT (**Fig. S1E**). Altogether, these results demonstrate that CD8 T cell-intrinsic Bhlhe40 is required for anti-PD-1 efficacy but is dispensable for response to anti-CTLA-4.

Bhlhe40 Is Enriched in Effector/Exhausted CD8 T Cells

To gain insights into the divergent effects of anti-PD-1 and anti-CTLA-4 therapies, we performed single-cell RNA sequencing (scRNAseq) on immune cells isolated from 1956 tumors of Bhlhe40-sufficient ($B^{f/f}$) mice, mice lacking Bhlhe40 only in CD8 T cells ($B^{\Delta CD8}$), and mice lacking Bhlhe40 in both CD4 and CD8 T cells ($B^{\Delta T}$) treated with control Ab, anti-PD-1, or anti-CTLA-4 (**Fig. S2A**). Live Thy1.2^{+} CD45^{+} and Thy1.2^{-} CD45^{+} immune cells were sorted, barcoded, and mixed at 60:40 ratio to enhance capture of less frequent lymphoid cells for scRNAseq. To further increase lymphocyte resolution by accumulating more lymphocytes, we performed an additional experiment under the same treatment conditions, this time focusing specifically on Thy1.2 CD45 lymphocytes from $B^{f/f}$ and $B^{\Delta CD8}$ mice (**Fig. S2A**). We then

integrated the scRNAseq data from both experiments for downstream analysis of CD4 and CD8 T cells (**Fig. S2B**).

Unsupervised clustering of *Cd3e*$^{+}$ *Cd8a*$^{+}$ cells from our scRNAseq experiment identified seven CD8 T cell clusters (plus two small clusters of non-CD8 T cells, which were removed from downstream analyses). These spanned a range of states and included activated effector or exhausted (PD1^{hi}_Eff_Ex; Nr4a1^{hi}_Eff_Ex; Cd39^{+} Eff_Ex; Tox^{hi}_Eff_Ex), cycling/proliferating cells (Eff_Cycling), progenitor exhausted (Tpex)-like/interferon-stimulated cells (Tpexlike_Ifn-Stim), and naïve/memory-like populations (Naïve_Mem) based on functional marker transcript expression and comparisons to published datasets[34,42-45] (**Figs. 2C-2G, S2C,** and **S3**).

Treatment with ICT reshaped the CD8 T cell compartment in a manner that was dependent on genotype and whether mice were treated with anti-PD-1 or anti-CTLA-4 **(Fig. S2E)**. We first noted that effector/exhausted clusters expressed the highest levels of *Bhlhe40* in B$^{f/f}$ mice. Among these, the PD1^{hi}_Eff_Ex cluster exhibited the highest inferred Bhlhe40 regulon activity by SCENIC analysis, whereas the Naïve_mem cluster showed the lowest regulon activity (**Figs. 2D-F, S2C,** and **S2D**). PD1^{hi}_Eff_Ex also expressed key effector molecules (e.g., *Ifng*, *Gzmb*, *Prf1*), as well as relatively high levels of inhibitory receptor transcripts (e.g., *Pdcd1* (PD-1), *Havcr2* (TIM-3), *Lag3*), which are induced upon TCR activation but become hallmarks of exhausted and/or dysfunctional CD8 T cells when their expression is high and sustained[46-50] (**Figs. S2C** and **S3**). Nr4a1^{hi}_Eff_Ex was noted for its expression of *Nr4a1* (Nur77), a gene upregulated proportionally to TCR signaling strength[51,52], as well as high levels of *Ifng*, *Gzmb*, and *Cd69* (**Figs. 2D, S2C,** and **S3**). Tox^{hi}_Eff_Ex was the smallest cluster and expressed high levels of *Tox*, encoding a transcription factor essential for enforcing exhausted/dysfunctional T cell states[53-56], in addition to *Pdcd1*, *Havcr2*, *Lag3*, and *Entpd1* (CD39) (**Figs. 2D, S2C,** and **S3**). Cells within this cluster also expressed *Slamf6* (Ly108) and *Tcf7*, which encodes the TCF-1

transcription factor that supports stem-like Tpex cells essential for sustained anti-PD-1 responses and for anti-CTLA-4-driven T cell memory[17,43,57-62]. Notably, expression of *Tcf7* was restricted to a subset of cells and was partially exclusive of *Tox* expression (**Figs. 2D** and **S2F**). Clusters Eff_Cycling was a proliferating cluster that expressed *Bhlhe40* at moderate levels, whereas Tpex-like_Ifn-stim expressed lower levels of *Bhlhe40* (**Fig. S2C**). Cluster Tpex-like_Ifn-stim displayed upregulation of interferon (IFN)-stimulated transcripts, high *Gzmk* expression, and also Tpex-associated transcripts such *Tcf7* and *Slamf6* **(Figs. S2C** and **S3**).

Bhlhe40 Regulates Neoantigen-Specific CD8 T Cell Responses to Anti-PD-1 and Supports IFN-γ Production

We assessed whether the differential tumor control observed with anti-PD-1 versus anti-CTLA-4 in the absence of CD8 T cell-intrinsic Bhlhe40 was reflected at the level of tumor-specific T cell responses. Anti-CTLA-4 increased the overall frequency of CD8 T cells in $B^{f/f}$ mice, while no significant changes were observed across other conditions (**Fig. 3A**). However, both anti-PD-1 and anti-CTLA-4 increased the frequency of tumor-specific CD8 T cells recognizing mutant Psmd6, an MHC class I (MHC-I) mutant NeoAg in the 1956 tumor[38] (**Fig. 3B**). Notably, anti-CTLA-4 drove this increase independently of CD8 T cell-intrinsic Bhlhe40, whereas anti-PD-1 selectively increased Psmd6-specific CD8 T cells in $B^{f/f}$ control mice and not in $B^{\Delta CD8}$ mice.

We previously found that CD8 T cells from mice lacking Bhlhe40 in both CD4 and CD8 T cells exhibited altered responses to ICT, including defects in IFN-γ expression[30]; however, it was unclear whether these changes were due to a CD8 T cell-intrinsic requirement for Bhlhe40 or reflected indirect effects stemming from its ablation in CD4 T cells. Our use of $B^{\Delta CD8}$ mice now demonstrate that some of these Bhlhe40-dependent changes, including reduced IFN-γ production, are at least partially attributable to CD8 T cell-intrinsic Bhlhe40. Specifically, cluster

Nr4a1^{hi}_Eff_Ex, which exhibited the highest levels of *Ifng* among CD8 T cell clusters (**Figs. S2C** and **S3**), as well as several other clusters showed reduced *Ifng* expression in B$^{\Delta CD8}$ mice compared to B$^{f/f}$ mice within the corresponding treatment groups (**Fig. S4A**). We observed an even more pronounced reduction of *Ifng* expression in mice lacking Bhlhe40 in both CD8 and CD4 T cells (B$^{\Delta T}$), suggesting that Bhlhe40 expression in CD4 T cells also supports *Ifng* production by CD8 T cells (**Fig. S4A**). At the protein level, although IFN-γ-positive cells as a percentage of CD8 T cells did not change significantly between B$^{f/f}$ and B$^{\Delta CD8}$ mice with anti-PD-1 treatment, the expression level of IFN-γ was significantly decreased based on mean fluorescence intensity (MFI) (**Fig. 3C**). Notably, reductions in IFN-γ production were observed not only with anti-PD-1—which fails to induce rejection in B$^{\Delta CD8}$ mice—but also with anti-CTLA-4, despite the latter still leading to tumor rejection in B$^{\Delta CD8}$ mice. Further, a significant decrease in IFN-γ^{+} TNF-α^{+} CD8 T cells was observed in B$^{\Delta CD8}$ mice compared to B$^{f/f}$ mice within comparable treatment groups (**Fig. 3C**). In addition to alterations in *Ifng*, *Il10* expression was increased in the clusters expressing the highest levels of *Il10* (PD1^{hi}_Eff_Ex and Nr4a1^{hi}_Eff_Ex) in B$^{\Delta CD8}$ mice (**Fig. S4B**), consistent with Bhlhe40's function as a transcriptional repressor of *Il10*[23,24,28].

Gene set enrichment analysis (GSEA) revealed that, under anti-PD-1 or anti-CTLA-4 treatment, multiple CD8 T cell clusters from B$^{\Delta CD8}$ mice exhibited significant negative enrichment of the Hallmark IFN-γ response gene set compared to B$^{f/f}$ controls, with several clusters also showing reduced IFN-α response signatures (**Figs. 3D, S5,** and **S6**). Reduced IFN-γ signatures likely reflect impaired IFN-γ production by Bhlhe40-deficient CD8 T cells, whereas diminished IFN-α response may represent secondary effects of altered CD8 T cell function. Notably, although IFN-γ response genes were reduced in B$^{\Delta CD8}$ mice under anti-CTLA-4 relative to B$^{f/f}$ controls, they remained relatively enriched compared to anti-PD-1-treated B$^{\Delta CD8}$ mice (**Fig. 3E**).

Bhlhe40 Shapes Effector and Exhausted CD8 T Cell States

We hypothesized that Bhlhe40 contributes to effector/exhausted phenotypes as we noted in several clusters, expression of not only *Ifng*, but also *Pdcd1*, *Lag3*, *Ctla4*, *Gzmk*, and the fractalkine receptor gene *Cx3cr1* were reduced in $B^{\Delta CD8}$ mice relative to $B^{f/f}$ controls (**Figs. S3** and **S4A**). These cells also showed increased expression of several immunoregulatory genes (*Cd5*, *Cd6*, *Ptprj*, and *Pag1*) (**Figs. S3** and **S4A**). We also observed changes that followed similar patterns in control Ab and anti-PD-1 conditions but diverged under anti-CTLA-4 treatment. Under anti-PD-1 treatment, induction of *Prf1* was attenuated in $B^{\Delta CD8}$ mice, which also showed lower baseline *Prf1* levels under control treatment, whereas anti-CTLA-4 treatment resulted in higher *Prf1* expression in $B^{\Delta CD8}$ compared to $B^{f/f}$ mice (**Figs. S3** and **S4A**). Similarly, *Tox* expression was reduced in anti-PD-1-treated $B^{\Delta CD8}$ mice, whereas anti-CTLA-4 reduced *Tox* expression to comparable levels in both $B^{f/f}$ and $B^{\Delta CD8}$ mice (**Fig. S4C**). A notable exception to the reduced expression of effector and exhaustion-associated genes was increased *Gzmb* expression in Bhlhe40-deficient CD8 T cells upon anti-PD-1 or anti-CTLA-4 treatment.

To better understand how Bhlhe40 shapes these phenotypes, we explored its relationship with CD8 T cell phenotype-defining transcriptional programs. Correlation analysis revealed an inverse relationship between *Bhlhe40* and *Tcf7*, *Sell*, *Id3*, *Bcl2*, *Cxcr3*, *Lef1*, *Slamf6*, and *Eomes*, genes associated with naïve, memory, and Tpex-like phenotypes (**Figs. 4A** and **S7A**). In contrast, *Bhlhe40* was associated with transcripts linked to T cell activation, survival, effector differentiation, and exhaustion including *Nr4a1*, *Junb*, *Jund*, *Bcl2a1b*, *Rgs16*, *Irf8*, *Rbpj*, and *Dusp5*[63-65] as well as inhibitory receptors (*Pdcd1*, *Ctla4*, *Lag3*, *Havcr2*, *Klrc1* [NKG2A]). Bhlhe40 was also correlated with genes related to cytotoxicity (*Nkg7*, *Srgn*) and costimulatory receptors (*Tnfrsf4* (OX40), *Tnfrsf9* (4-1BB), *Icos*), and *Hif1a*, a TCR-induced transcript whose stability is enhanced under hypoxic conditions, together with the downstream HIF1-responsive gene *Hilpda* (**Figs. 4A** and **S7A**).

Given the strong inverse correlation between *Bhlhe40* and *Tcf7*-associated naïve/memory and Tpex programs, we next examined how loss of Bhlhe40 affected these states. The Naïve_mem cluster expressed the highest levels of *Tcf7* (**Figs. S3, S8A,** and **S8B**), and this cluster was markedly expanded in control Ab-treated $B^{\Delta CD8}$ mice compared to $B^{f/f}$ mice (**Fig. S2E**). Under anti-PD-1 treatment, *Tcf7* expression within the Naïve_mem cluster was also elevated in $B^{\Delta CD8}$ mice. Moreover, in the absence of ICT, increased *Tcf7* expression in $B^{\Delta CD8}$ mice was observed across several CD8 T cell clusters in which only a small fraction of cells expressed *Tcf7*. A similar pattern was noted for *Bach2*, which encodes a transcriptional repressor that enforces stem-like and Tpex states[66] (**Fig. S8B**). Consistent with these findings, the Naïve_mem cluster showed the lowest putative Bhlhe40 regulon activity (**Fig. S2D**). Trajectory analysis further supported this relationship, as Monocle3 analysis starting from Naïve_mem revealed opposing dynamics of *Bhlhe40* and *Tcf7* across pseudotime (**Figs. 4B** and **4C**). At the protein level, intratumoral Tpex/Tpex-like PD-1□ TCF-1□ CD8 T cells were significantly expanded in $B^{\Delta CD8}$ mice under both control Ab and anti-PD-1 treatment conditions compared to $B^{f/f}$ mice (**Fig. 4D**).

We next sought to determine whether Bhlhe40 directly interacts with regulatory regions of genes associated with these states by performing CUT&RUN to map Bhlhe40 binding sites in intratumoral CD8 T cells from WT mice treated with control Ab, anti-PD-1, or anti-CTLA-4. Consistent with this hypothesis, Bhlhe40 occupied distal intergenic regions of *Tcf7* under control conditions (−16 kb and −35 kb from the transcription start site [TSS]) and under anti-PD-1 treatment (−35 kb from the TSS) (**Fig. 4E** and **Table S6-S7**). Comparison with published datasets revealed that the −16 kb and −35 kb regions are consistent with Bhlhe40 CUT&RUN peaks in CD8 T cells from LCMV-infected mice[67], whereas the −35 kb region also overlaps a Bhlhe40 ChIP-seq peak identified in *in vitro* polarized CD4 T cells[24]. We also identified five Bhlhe40 CUT&RUN peaks within the *Bach2* locus under control treatment conditions and four under anti-PD-1 treatment

(**Fig. 4F** and **Table S6-S7**). Together, these findings support a model in which Bhlhe40 directly restrains *Tcf7*- and *Bach2*-associated Tpex-like programs while promoting effector differentiation in tumor-infiltrating CD8 T cells.

Bhlhe40 Is Required for Differentiation Toward Conventional Effector and Exhausted CD8 T Cell States

To further examine how Bhlhe40 loss influences the balance between effector/exhausted and Tpex-like CD8 T cell phenotypes, we crossed OT-I TCR transgenic mice with Bhlhe40$^{-/-}$ mice to generate Bhlhe40-deficient OT-I (B$^{-/-}$ OT-I) mice. To ensure *in vivo* relevance of this system, we first evaluated whether Bhlhe40 was required for OT-I CD8 T cell-mediated tumor control in an adoptive cell therapy model. Splenocytes from B$^{+/+}$ OT-I and B$^{-/-}$ OT-I mice were stimulated with SIINFEKL peptide, the ovalbumin (OVA)-derived cognate epitope presented by H2-K^{b}. Stimulated B$^{+/+}$ or B$^{-/-}$ OT-I cells were then isolated and adoptively transferred into mice bearing B16-OVA melanomas. While transfer of B$^{+/+}$ OT-I CD8 T cells delayed tumor outgrowth, B$^{-/-}$ OT-I CD8 T cells failed to reduce tumor growth (**Fig. 4G**). We then used an *in vitro* culture assay to compare transcript expression of effector and exhaustion markers (*Pdcd1*, *Lag3*, *Havcr2*, *Ifng*) and memory-associated markers (*Tcf7*, *Il7r*) in B$^{+/+}$ and B$^{-/-}$ OT-I T cells under acute and chronic stimulation conditions. As expected, chronic stimulation led to increased *Pdcd1*, *Lag3*, and *Havcr2* expression and reduced *Tcf7* and *Il7r* expression in B$^{+/+}$ OT-I cells compared to acute stimulation (**Fig. 4H**). However, under both stimulation conditions, B$^{-/-}$ OT-I cells exhibited reduced expression of *Pdcd1*, *Lag3*, *Havcr2*, and *Ifng*, while *Tcf7* and *Il7r* expression remained significantly elevated relative to B$^{+/+}$ OT-I cells. Collectively, these results indicate that Bhlhe40 is required for proper transcriptional programming and functional differentiation of effector and exhausted CD8 T cells.

Bhlhe40 Sustains Glycolytic and Mitochondrial Metabolic Fitness in CD8 T Cells

Given that effector differentiation and cytokine production are tightly linked to metabolic rewiring, we next examined whether Bhlhe40 influences the metabolic profile of intratumoral CD8 T cells in 1956 tumor-bearing mice. Pathway enrichment analysis of genes correlated with *Bhlhe40* highlighted glycolysis-associated metabolic programs (**Figs. 4A, S7A,** and **S7B**), consistent with the metabolic rewiring of activated CD8 T cells. Key glycolytic genes such as *Aldoa*, *Gapdh*, *Pgk1*, and *Eno1*, were markedly reduced in anti-PD-1- or anti-CTLA-4- treated $B^{\Delta CD8}$ mice compared to $B^{f/f}$ mice, particularly within the effector/exhausted clusters that also display the highest *Bhlhe40* expression (**Figs. 5A, S3,** and **S9A**). GSEA also showed negative enrichment of glycolysis-associated gene sets across several effector clusters in $B^{\Delta CD8}$ mice treated with anti-PD-1 or anti-CTLA-4 relative to $B^{f/f}$ counterparts **(Figs. 5B, S5,** and **S6)**. Notably, in $Bhlhe40^{\Delta T}$ mice lacking Bhlhe40 in both CD4 and CD8 T cells, glycolytic gene expression was more severely impaired than in $B^{\Delta CD8}$ mice, suggesting a role for Bhlhe40 in CD4 T cells in facilitating CD8 T cell glycolytic fitness (**Fig. S9B**). Although we did not observe as extensive a reduction in OXPHOS-related transcripts in Bhlhe40-deficient CD8 T cells (**Fig. S9C**), GSEA revealed significantly decreased enrichment of OXPHOS-associated gene sets in several CD8 T cell clusters from anti-PD-1- and anti-CTLA-4- treated $B^{\Delta CD8}$ mice (**Figs. S5** and **S6**).

To determine whether these transcriptional changes corresponded to functional metabolic alterations, we performed Seahorse extracellular flux analysis on intratumoral CD8 T cells. Consistent with our scRNAseq-based indications, Bhlhe40-deficient CD8 T cells from anti-PD-1-treated $B^{\Delta CD8}$ mice exhibited significantly reduced ATP production from both glycolysis and mitochondrial OXPHOS (**Fig. 5C**) and ECAR/OCR time-course analyses similarly revealed diminished glycolytic activity and impaired OXPHOS in $B^{\Delta CD8}$ mice (**Fig. 5D**). In contrast, CD8 T cells from anti-CTLA-4-treated $B^{\Delta CD8}$ mice showed a significant reduction in glycolytic ATP production while largely maintaining mitochondrial ATP production (**Figs. 5C** and **5D**). These

findings reveal that CD8 T cell-intrinsic Bhlhe40 is indispensable for maintaining glycolytic and mitochondrial ATP-generating metabolic pathways under anti-PD-1 therapy, whereas anti-CTLA-4 treatment uncovered a more selective reliance on Bhlhe40 for glycolysis but not mitochondrial respiration.

T Cell-Intrinsic Bhlhe40 Sustains Anti-CTLA-4-Driven Th1 Responses and Tumor Rejection

Having defined the CD8 T cell defects caused by Bhlhe40 loss, we next asked whether differences in CD4 T cell responses could explain the divergent therapeutic outcomes, namely, that anti-CTLA-4 remains effective in $B^{\Delta CD8}$ mice but fails in $B^{\Delta T}$ mice. Notably, in both the 1956 and Y1.7LI tumor models, anti-CTLA-4 requires contributions from both CD4 and CD8 T cells for tumor control[30,41]. Therefore, the preserved efficacy of anti-CTLA-4 in $B^{\Delta CD8}$ mice cannot be interpreted as CD8 T cell dispensability; rather, it suggests that CD4 T cell-driven effects may compensate for Bhlhe40 loss in CD8 T cells. Consistent with prior studies[20,21,30,41], anti-CTLA-4 more profoundly affected conventional CD4 T helper cells (CD4 T cells) and regulatory T cells (Tregs) relative to anti-PD-1 (**Figs. S10A** and **S10B**). Whereas anti-PD-1 did not alter the frequency of CD4 T cells in either $B^{f/f}$ mice or $B^{\Delta CD8}$ mice, anti-CTLA-4 increased the frequency in both genotypes (**Fig. S10A**). As expected with anti-CTLA-4 clone 9D9 [68], treatment reduced Tregs, an effect that was independent of Bhlhe40 expression in CD8 T cells, as measured by both flow cytometry and scRNA-seq (Treg_1 cluster) **(Figs. 6A, S10A,** and **S10B)**. We next examined effector CD4 T cell populations that might contribute to anti-CTLA-4-mediated tumor control. scRNA-seq analysis identified several clusters of effector CD4 T cells, including multiple T helper 1 (Th1) populations characterized by *Ifng*, *Tbx21* (Tbet), and *Bhlhe40* expression **(Figs. 6B, S10C,** and **S10D)**. Amongst these, $ICOS^{hi}Bhlhe40^{hi}$_Th1_6 expressed the highest levels of *Bhlhe40, Tnf,* and *Ifng* among CD4 T cells, along with *Icos* (under anti-CTLA-4 treatment), *Tbx21*, and *Pdcd1* **(Figs. 6B, S10C,** and **S10D)**. This cluster also

expressed *Bcl6*, indicating some transcriptional features of T follicular helper cells (Tfh) **(Fig. S10D)**. Gzmk^{+}_Th1_8 expressed Th1 markers (e.g., *Tbx21*, *Ifng*) but also displayed high expression of *Gzmk*, along with moderate expression of *Tcf7* and *Slamf6* **(Fig. S10D)**. Comparative analysis with published datasets[45,69] indicated that these murine Th1 subsets share transcriptional features with cytotoxic or highly activated effector populations in human cancer (**Fig. 6C**).

As expected[20,41,70-72], anti-CTLA-4 promoted expansion of ICOS$^{\mathbf{hi}}$Bhlhe40$^{\mathbf{hi}}$_Th1_6 and ICOS^{+}Bhlhe40^{+}_Th1_7 **(Figs. 6D** and **S10B)**. These populations expanded not only in B$^{f/f}$ and B$^{\Delta CD8}$ mice, but also in B$^{\Delta T}$ mice, although the magnitude of expansion varied by genotype. Despite this expansion, several transcriptomic alterations were observed in mice with disrupted Bhlhe40 expression in both CD8 and CD4 T cells (B$^{\Delta T}$ mice) **(Figs. S10C** and **S10D)**. Notably, when comparing *Ifng* expression within CD4 T cells across treatments and knockout conditions, two important patterns emerged. First, anti-CTLA-4 induced a higher frequency of Th1 CD4 T cells expressing elevated levels of *Ifng* compared to anti-PD-1, and this increase was observed in both B$^{f/f}$ and B$^{\Delta CD8}$ mice—treatment settings in which anti-CTLA-4-driven tumor rejection occurs (**Figs. 2B, 6D, 6E, S10C,** and **S10D**). Second, in the absence of Bhlhe40 in CD4 T cells (B$^{\Delta T}$ mice), *Ifng* expression was markedly reduced under all treatment conditions, including anti-CTLA-4, and in these mice, the efficacy of anti-CTLA-4 (as well as anti-PD-1) was lost (**Figs. 2B, 6D, 6E, S10C,** and **S10D**).

Interestingly, we observed a modestly decreased expression of glycolytic transcripts in CD4 effector T cells from B$^{\Delta CD8}$ mice (**Fig. 6F**). In contrast, CD4 T cells from B$^{\Delta T}$ mice, lacking Bhlhe40 in both CD4 and CD8 T cells, displayed striking reductions in glycolytic transcript expression compared to B$^{f/f}$ mice, including in anti-CTLA-4-treated conditions. These findings suggest that CD8 T cell-intrinsic Bhlhe40 contributes indirectly to maintaining glycolytic

transcript expression in CD4 effector T cells, whereas loss of Bhlhe40 across all T cell compartments leads to a more profound defects in metabolic transcript expression.

T Cell-Intrinsic Bhlhe40 Shapes Macrophage Phenotypes

Our findings thus far indicate that Bhlhe40 orchestrates CD8 and CD4 T cell effector programs that are differentially required for anti-PD-1 and anti-CTLA-4 efficacy. Because we previously showed that anti-PD-1 and anti-CTLA-4 promote T cell-driven intratumoral macrophage remodeling, shifting from M2-like CX3CR1^{+} macrophages to M1-like iNOS^{+} macrophages[21,41,73], we asked whether T cell-intrinsic Bhlhe40 also governs ICT-driven changes in intratumoral macrophages. We identified by scRNAseq multiple monocyte/macrophage clusters, including CX3CR1^{+} macrophage clusters expressing *Cx3cr1* and *Mrc1* (CD206) as well as distinct clusters expressing *Nos2* (iNOS) (**Figs. S11A-S11B**). Both scRNAseq and flow cytometry revealed a marked impairment in ICT-driven macrophage remodeling in B$^{\Delta CD8}$ mice, and an even more pronounced defect in B$^{\Delta T}$ mice lacking Bhlhe40 in both CD4 and CD8 T cells (**Figs. S11C-S11E**). Whereas anti-PD-1 or anti-CTLA-4 reduced the frequency of CX3CR1^{+} macrophages in B$^{f/f}$ mice, this reduction was absent in B$^{\Delta CD8}$ and B$^{\Delta T}$ mice, which instead exhibited elevated frequencies of CX3CR1□ macrophages under both control Ab and ICT conditions (**Figs. S11D** and **S11E**). This was also reflected by transcript expression of markers enriched on pro-tumoral macrophages (**Fig. S11C**), including *Trem2*, which we and others have shown is a therapeutic target on immunosuppressive macrophages[41,74,75]. Anti-PD-1 and especially anti-CTLA-4 expanded iNOS^{+} macrophages in B$^{f/f}$ mice, whereas the frequency of iNOS^{+} macrophages was severely reduced in B$^{\Delta CD8}$ mice, with an even greater reduction occurring in B$^{\Delta T}$ mice (**Fig. S11E**). These findings indicate that Bhlhe40 expression in CD8 T cells, and more critically, in both CD4 and CD8 T cells, is required for ICT-induced macrophage remodeling, linking T cell-intrinsic Bhlhe40 to the shift from immunosuppressive CX3CR1□ macrophages to proinflammatory iNOS□ macrophages within the TME.

Bhlhe40 Correlates with Effector and Exhaustion Programs in Human Intratumoral CD8 T Cells

To relate our preclinical findings to human tumors, we next reanalyzed scRNAseq datasets[34,42,76,77] from human cancer patients. These analyses revealed expression patterns between *BHLHE40* and several transcripts associated with T cell differentiation and functional programs similar to those observed in mice. In melanoma (Sade-Feldman et al. and Minowa et al.) and basal cell carcinoma (Yost et al.) datasets, gene-correlation analyses showed that *BHLHE40* expression was positively correlated with *TOX*, *PDCD1*, *ENTPD1*, *HAVCR2*, *LAG3*, *IFNG*, and *GZMB* (**Fig. 7A**). In contrast, *BHLHE40* exhibited negative correlation with *TCF7*, as well as *SELL* (CD62L) and *IL7R*. Consistent with these correlations, in triple-negative breast cancer (TNBC), *BHLHE40* was expressed in activated CD8 T cell clusters expressing *TOX* and *IFNG* (**Figs. S8C** and **S8D**).

Next, we further analyzed the basal cell carcinoma dataset from Yost et al.[76], which included pre- and post-treatment samples from responders and non-responders treated with PD-1 blockade. As expected, *BHLHE40* expression was highest in the CD8 T cell clusters classified by Yost et al. as 'activated' or 'exhausted,' whereas the 'memory' CD8 T cell cluster exhibited lower *BHLHE40* levels and higher *TCF7* expression (**Figs. 7B**). Notably, within these activated and exhausted CD8 T cell populations, *BHLHE40* expression was higher in responders compared with non-responders at pre-treatment (**Fig. 7C**). Following treatment, exhausted CD8 T cells showed elevated *BHLHE40* expression in responders. To determine whether *BHLHE40* expression associated with clinical outcome within stable TCR lineages, we analyzed persistent clonotypes present at both pre-treatment and post-treatment timepoints as defined in Yost et al. Persistent CD8 T cell clones from responders exhibited significantly higher *BHLHE40* expression compared to those from non-responders at pre-treatment (**Fig. 7D**). Collectively, our murine and

human analyses identify Bhlhe40 as a central T cell-intrinsic regulator that couples effector and exhausted CD8 T cell differentiation and Th1 CD4 T cell function to macrophage remodeling and ICT efficacy, and further show that higher *BHLHE40* expression within tumor CD8 T cells associates with clinical response to PD-1 blockade. Further, these findings suggest that differential dependence on CD8 T cell-intrinsic Bhlhe40 contributes, at least in part, to the distinct mechanisms by which anti-PD-1 and anti-CTLA-4 mediate tumor rejection.

DISCUSSION:

Our study identifies Bhlhe40 as a transcriptional coordinator with distinct, therapy-specific requirements in CD4 and CD8 T cells during ICT. Mechanistically, Bhlhe40 promotes the acquisition of effector and exhausted CD8 T cell states and sustains IFN-γ production, while supporting both glycolytic and mitochondrial programs. Consistent with this, loss of Bhlhe40 skews CD8 T cells towards more Tpex-like states with elevated TCF-1 expression and reduced acquisition of terminal effector features, particularly under anti-PD-1 treatment and in the absence of ICT. Although the relationship between Bhlhe40 and several transcripts/proteins associated with CD8 T cell function may be indirect, some of the observed changes are likely attributable to Bhlhe40-mediated transcriptional activation or repression of specific target genes. For example, Bhlhe40 has been shown to positively regulate *Ifng* and negatively regulate *Il10*[23,24,28], consistent with our findings. In addition, *Tcf7* contains several E-box motifs within its regulatory regions[78] and CUT&RUN analyses of intratumoral CD8 T cells revealed Bhlhe40 enrichment at regulatory regions of *Tcf7* under control and anti-PD-1 treatment conditions. This raises the possibility that Bhlhe40 may not only be co-expressed with markers of activated, effector, or exhausted CD8 T cells due to shared upstream signals such as TCR stimulation, but may also contribute directly to driving CD8 T cell differentiation toward effector and exhausted phenotypes. Collectively, our findings support a model in which Bhlhe40 functions as a transcriptional switch that drives effector (and exhausted) phenotypes in tumors in part by

modulating TCF-1 expression. Consistent with this model, Wu et al.[79] recently demonstrated using in vitro chronic stimulation and chronic infection models that Bhlhe40 regulates a differentiation checkpoint between progenitor and intermediate exhausted CD8 T cells.

Anti-PD-1 and anti-CTLA-4 each utilize both shared and distinct mechanisms[20,21,41]. Anti-PD-1 predominantly expands and sustains effector function from a PD-1^{+} TCF-1 progenitor (Tpex) CD8 T cell pool, as terminally exhausted cells are epigenetically constrained and minimally reinvigorated[47], whereas anti-CTLA-4, directly and via CD4 T cell help, enhances CD8 T cell priming/expansion with more memory-like and less terminally exhausted features (increased TCF-1 and decreased TOX)[11,20,21,58,60,80,81].

These differences provide a basis for the differential requirement for Bhlhe40 in CD8 T cells during anti-PD-1 versus anti-CTLA-4 therapy. Whereas anti-PD-1 efficacy likely depends on Bhlhe40 to drive the transition of CD8 Tpex cells into effector (and exhausted) states, anti-CTLA-4 may rely less on CD8 T cell-intrinsic Bhlhe40 and instead promote expansion of CD8 T cells with more memory-like or less terminal effector/exhausted features. Nevertheless, loss of CD8 T cell-intrinsic Bhlhe40 did cause functional alterations, including reduced CD8 T cell-derived IFN-γ, during anti-CTLA-4 treatment, although anti-CTLA-4 still expanded Psmd6-specific CD8 T cells and maintained tumor rejection. This preservation of tumor control may be due in part to compensatory actions of CD4 T cells. We recently found that IFN-γ^{+} Th1-like ICOS^{+} CD4 T cells induced by anti-CTLA-4[20,71] highly express Bhlhe40 [41], consistent with prior reports that Bhlhe40 promotes conventional Th1 differentiation and sustains IFN-γ production in autoimmune and infection settings[23,32,82]. These anti-CTLA-4-induced ICOS^{+} Th1-like cells likely contribute to tumor control in B$^{\Delta CD8}$ mice, where CD8 T cell function is compromised. In contrast, mice lacking Bhlhe40 in both CD4 and CD8 T cells failed to respond to either ICT modality, highlighting the cooperative roles of these subsets in orchestrating anti-tumor

immunity. Together, these findings indicate that the contribution of Bhlhe40 to ICT responses is not uniform across T cell subsets or therapeutic modalities, but instead reflects differential mechanisms engaged by anti-PD-1 versus anti-CTLA-4.

Importantly, the phenotypic and functional impairments observed in CD8 T cells lacking Bhlhe40 were accompanied by defects in ICT-driven remodeling of the tumor myeloid compartment from CX3CR1^{+} macrophages to iNOS^{+} macrophages. These CX3CR1□ macrophages likely constitute a large fraction of M2-like tumor-associated macrophages, often co-expressing CD206, C1q, ApoE, TREM2, etc., although marker usage and nomenclature varies across studies[14,19-21], whereas iNOS^{+} macrophages are consistent with inflammatory M1-like macrophages. Notably, the relatively greater expansion of iNOS^{+} macrophages observed with anti-CTLA-4 compared to anti-PD-1 in CD8 T cell Bhlhe40-deficient mice may reflect CD4 T cell-derived IFN-γ and Th1-like help, whereas combined loss of Bhlhe40 in both CD4 and CD8 T cells profoundly impaired macrophage remodeling, even under anti-CTLA-4 therapy.

Our data also link Bhlhe40 to metabolic programming in a partially therapy-dependent manner. Under anti-PD-1 treatment, Bhlhe40-deficient CD8 T cells exhibited marked reductions in both glycolytic and OXPHOS capacity, with reduced mitochondrial respiration consistent with prior work implicating Bhlhe40 in sustaining mitochondrial fitness during anti-PD-1 therapy[26]. Under anti-CTLA-4 treatment, Bhlhe40-deficient CD8 T cells retained OXPHOS but displayed reduced glycolytic activity. Interestingly, loss of Bhlhe40 in CD8 T cells also impaired glycolytic transcript expression in CD4 effector T cells, reflecting alterations in CD8 T cells that either directly influence CD4 T cells or reshape the TME in ways that secondarily impact CD4 T cells. Notably, in B$^{\Delta T}$ mice lacking Bhlhe40 in both CD4 and CD8 T cells, glycolytic transcript expression in CD4 T cells was markedly reduced across treatment conditions. ICT-induced, Bhlhe40-dependent T cell-driven changes to tumor metabolism may also influence T cell

metabolic fitness, as increased tumor glucose consumption and lactate production could further constrain T cell glycolysis by acidifying the TME[83].

These observations align with the well-established requirement for robust glycolytic and mitochondrial programs to support effector cytokine production, cytotoxicity, and persistence of T cells in the TME[84-86]. In particular, glycolysis supports effector responses, whereas mitochondrial metabolism supports sustained function and long-term survival under conditions of chronic stimulation[83,85-87]. Given the requirement for T cells to upregulate glycolysis upon effector differentiation, it is notable that signals downstream of TCR activation and costimulation that drive metabolic reprogramming also induce Bhlhe40 expression, placing Bhlhe40 at the interface between activation-induced metabolic enhancement and effector programming.

Analysis of human cancer datasets revealed that *BHLHE40* is enriched in tumor-reactive and activated/exhausted CD8 T cells across multiple tumor types, inversely correlated with *TCF7*, and positively associated with *TOX*, *GZMB*, and *IFNG*. Moreover, analysis of the Yost et al. dataset[76] revealed that persistent TCR clonotypes—defined as clones present at both pre- and post-treatment timepoints—exhibited higher *BHLHE40* expression in responders compared to non-responders before PD-1 blockade. These findings suggest that *BHLHE40* marks an effector-biased intratumoral CD8 T cell population with enhanced capacity to persist through therapy and sustain anti-tumor immunity. Together, these observations support the relevance of our murine findings to human ICT responses and suggests that Bhlhe40 expression could serve as a biomarker for T cell differentiation state and functional competence in the TME.

Collectively, our findings position Bhlhe40 as a subset- and therapy-specific regulator of ICT responses, integrating effector programming, metabolic fitness, and myeloid remodeling to

provide mechanistic insight into the distinct modes of action of anti-PD-1 and anti-CTLA-4. While multiple transcription factors influence T cell programs relevant to ICT, our study provides one of the clearest demonstrations of a transcriptional regulator that imposes T cell subset-specific requirements for anti-PD-1 versus anti-CTLA-4 efficacy, resulting in complete loss of one therapy while fully sparing the other. From a translational perspective, these results suggest that strategies to sustain or enhance Bhlhe40 activity, particularly in CD8 T cells during PD-1 blockade, may improve therapeutic efficacy. Conversely, the ability of CD4 T cells to preserve anti-CTLA-4 efficacy despite CD8 T cell impairment suggests opportunities to harness or amplify these complementary pathways to improve immunotherapy responses.

MATERIALS AND METHODS:

Mice

All mice used were on a C57BL/6 background. Wild type C57BL/6J, *CD4-Cre* (B6.Cg-Tg(Cd4-cre)1Cwi/BfluJ)[36]: JAX stock #022071, *CD8 E8I-Cre* (B6.Tg(Cd8a-cre)1Itan/J)[37]: JAX stock #008766, *Bhlhe40*$^{-/-}$ (B6.129S1(Cg)-Bhlhe40tm1.1Rhli/MpmJ): JAX stock #029732, and OT-I TCR transgenic (Tg(TcraTcrb)1100Mjb/J): JAX stock #003831 mice were purchased from Jackson Labs. All *in vivo* experiments used 8–12-week-old female or male (to match the sex of the tumors), all mice were housed in our specific pathogen-free animal facility. *Bhlhe40*$^{f/f}$ mice have been previously reported[23,24,30,88]. For experiments using conditional Bhlhe40 KO mice, *Bhlhe40*$^{f/f}$ littermates or *CD8 E8I-Cre Bhlhe40*$^{+/+}$ mice were used as controls. All studies were performed in accordance with procedures approved by the Institutional Animal Care and Use Committee (IACUC) at The University of Texas MD Anderson Cancer Center, an AAALAC accredited institution.

Tumor lines

The 1956 MCA-induced sarcoma line used in this study was generated in female wild type C57BL/6 mice and were banked as low-passage tumor cells as previously described[89] and were

obtained from Robert Schreiber (Washington University in St. Louis School of Medicine). Y1.7LI is a melanoma line derived from the $Braf^{V600E}$ $Cdkn2a^{-/-}$ $Pten^{-/-}$ YUMM1.7 line[40] engineered to express mLama4, an H2-K^b-restricted MHC class I neoantigen, and mItgb1, an I-A^b-restricted MHC class II neoantigen, as previously described[41]. Tumor lines from the same cryopreserved stocks that were used in this study tested were authenticated and found to be free of non-mouse cells by STR profiling (IDEXX CellCheck™ mouse 19 plus *Mycoplasma* spp. testing) and confirmed free of common mouse pathogens and mycoplasma by IDEXX IMPACT™ I mouse pathogen testing.

Tumor transplantation

1956 MCA sarcoma cells, B16-F10-OVA (B16-OVA) melanoma cells, and Y1.7LI melanoma cells were from frozen stocks and propagated in R-10 plus BME media [RPMI media (Hyclone) supplemented with 1% L-glutamine, 1% penicillin-streptomycin, 1% Na Pyruvate, 0.5% Na Bicarbonate, 0.1% 2-Mercaptoethanol, and 10% FCS (Hyclone)]. Upon thawing, tumor lines were passaged 3-5 times before experimental use. Prior to injection, cells were washed extensively, resuspended at a concentration of 6.67×10^6 cells per mL in endotoxin-free PBS for 1956 and at a concentration of 3.33×10^6 cells per mL in endotoxin-free PBS for B16-OVA and Y1.7LI and then 150 μl (1×10^6 cells per mouse for 1956 and 0.5×10^6 cells per mouse for B16-OVA and Y1.7LI) injected subcutaneously into the flanks of recipient mice. Tumor cells were >90% viable at the time of injection as assessed by trypan blue exclusion. Tumor growth was quantified by caliper measurements and expressed as the average of two perpendicular diameters.

Tumor harvest

Established tumors were isolated from mice, minced and treated with 1 mg/ml type IA collagenase (Sigma) in HBSS (Hyclone) for 45 minutes at 37 °C. Cells were washed thrice. Red blood cells were lysed using ACK lysis buffer (Gibco). To remove aggregates and clumps, cells were passed through a 40-micron strainer.

Immune checkpoint therapy

Mice were treated intraperitoneally with 200 μg of anti-PD-1 or anti-CTLA-4 on days 3, 6, 9 post-tumor transplant for 1956 and on days 7, 10, 13, 16, and 21 for Y1.7LI. For controls, mice were injected with 200 μg of isotype control antibodies.

***In Vivo* antibodies**

Anti-PD-1 (rat IgG2a clone RMP1-14) and anti-CTLA-4 (murine IgG2b clone 9D9) immune checkpoint antibodies were purchased from Leinco Technologies. Isotype control antibodies (rat IgG2a clone 1-1, mouse IgG2a clone OKT3, and rat IgG2b clone 1-2) were purchased from Leinco Technologies. All *in vivo* antibodies purchased from Leinco were "*In vivo* Platinum"-grade and were verified free of mouse pathogens (IDEXX IMPACT^{TM} I mouse pathogen testing).

Quantitative RT-PCR

RNA was extracted from sorted T cells using RNAeasy Plus Mini Kit (Qiagen). 1 μg of RNA was reverse-transcribed and subjected to qPCR using the SuperScript III Platinum Two-Step qRT-PCR Kit with SYBR Green (Invitrogen). qPCR was performed on the StepOne Real-Time PCR System (Applied Biosystems). Each sample was run in triplicate for each gene and the cDNA from each sample was divided equally per reaction in a 20 μl volume. The qPCR conditions were as follows: 50°C for 2 minutes and 95°C for 2 minutes, followed by 40 cycles of 95°C for 15 seconds and 60°C for 30 seconds. Melting curve analysis was performed to confirm a single amplicon. Differences in gene expression were determined using the equation $2^{-\Delta\Delta Ct}$, where the Ct value for *Gapdh* control was subtracted from the Ct value of *Bhlhe40* the to yield the ΔCt value. For each sample, the ΔCt value *Bhlhe40* done in triplicate was averaged and compared to give one ΔΔCt value per sample. Mouse quantitative RT-PCR primers for *Bhlhe40* were as follows: forward primer-5' ACGGAGACCTGTCAGGGATG3' and reverse primer-5'GGCAGTTTGTAAGTTTCCTTGC3'. Mouse quantitative RT-PCR primers for *Gapdh* were

as follows: forward primer-5'AGGTCGGTGTGAACGGATTTG3' and reverse primer-5'TGTAGACCATGTAGTTGAGGTCA3'.

Single-cell RNA Sequencing

Antibody hashing for multiplexing and single-cell RNA sequencing library preparation

Antibody hashing and multiplexing was utilized for scRNAseq. For the scRNAseq Experiment #1 and Experiment #2, cell labeling was performed according to an adapted BioLegend cell hashing protocol (TotalSeq™-C Antibodies and Cell Hashing with 10x Single Cell 5' Reagent Kit v1.1 Protocol, BioLegend). Single cell suspensions of harvested tumors from treated mice of different groups were resuspended in BioLegend Cell Staining Buffer containing Fc block and then surface stained with an antibody master mix consisting of anti-CD45.2/PE, anti-CD90.2/Thy1.2-PE-Cy7, and live/dead dye (NIR) and then barcoded antibodies with unique hashtags were added according to Supplement Table 1. Hashtag antibodies were used at a concentration of 1 μg per 2 million cells. Cells were then washed 3X with BioLegend Cell Staining Buffer and pooled for single-cell library generation and CITE-seq (cellular indexing of transcriptomes and epitopes by sequencing) through multiplexing. Cells were counted on a Countess 3 FL automated cell counter (Life Technologies) and viabilities were determined using trypan blue exclusion assay. Cell capture processing and gene expression and feature barcode library preparations were performed following 10X Genomics' guidelines for 5' scRNAseq by encapsulating sorted live $CD45^+$ tumor infiltrating cells [CG000330_Chromium Next GEM Single Cell 5' v2 (Dual Index) with Feature Barcode technology-Rev F]. QC steps after cDNA amplification and library preparation steps were carried out by running ThermoFisher Qubit HS dsDNA Assay along with Agilent (Santa Clara, CA) HS DNA Bioanalyzer for concentration and quality assessments, respectively. Library sample concentrations were verified using qPCR using a KAPA Biosystems KAPA Library Quantification Kit prior to pooling. Libraries were normalized to 5 nM for pooling. The pool was sequenced using a NovaSeq6000 S4-XP, 200-

cycle flow cell lane. The run parameters used were 26 cycles for read 1, 90 cycles for read2, 10 cycles for index1, and 10 cycles for index2 as stipulated in the protocol mentioned above.

Single-cell RNA sequencing alignment, barcode assignment, and UMI Counting

The Cell Ranger Single-Cell Software Suite available at https://support.10xgenomics.com/single-cell-gene-expression/software/overview/welcome was used to perform sample demultiplexing, barcode processing and single-cell 5' counting. “Cellranger mkfastq” was used to demultiplex raw base call files from the NovaSeq6000 sequencer, into sample-specific fastq files. Files were demultiplexed with 81.9% to 97.1% perfect barcode match, and 90%+ q30 reads. Afterward, fastq files for each sample were processed with “Cellranger count”, which was used to align samples to mm10 genome, filter and quantify. For each sample the recovered-cells parameter was specified as 10,000 cells that we expected to recover for each individual library.

Preprocessing analysis with Seurat package

The Seurat pipeline was applied to each dataset following tutorial specifications from [https://satijalab.org/seurat/articles/archive; version 3.2] and [https://hbctraining.github.io/scRNA-seq_online/]. QC process was performed for each experiment and group separately. Genes that were expressed in less than 3 cells and cells that contained less than 500 transcripts (UMI’s), or had less than 250 and more than 6500 genes, or more than 10% of mitochondrial transcripts, were excluded. Data were normalized using LogNormalize method. Potential doublets were removed by using scDblFinder package (1.16.0). For generating integrated CD8 T cell object, we used gene expression: *Cd3e* > *0*, *Cd8a* > 0 & *Cd4* = 0, similar for generating CD4 T cell object we used: *Cd3e* > *0, Cd4* > 0 & *Cd8a* = 0. All Cd8 and Cd4 data from all groups and experiments were integrated into a single CD8 or CD4 Seurat object. Expression matrix from all group were integrated using batch effect correction algorithm implemented in the Seurat V5 pipeline, employing anchor-based reciprocal principal component analysis (RPCA). Briefly, repeatedly variable genes across groups were selected by using ‘SelectIntegrationFeatures’ function. ScaleData and RunPCA were performed using these

genes. Next, anchors were identified with 'FindIntegrationAnchors' and integration was performed using these anchors through 'IntegrateData'. Unsupervised graph-based clustering was then performed on the integrated dataset. A UMAP dimensional reduction was performed on the scaled matrix (with most variable genes only) using first 40 PCA for CD8 and 50 PCA for CD4 components to obtain a two-dimensional representation of the cell states. For clustering, we used the function FindClusters that implements SNN (shared nearest neighbor) modularity optimization-based clustering algorithm.

Identification of cluster-specific genes and marker-based classification

To identify marker genes, the FindAllMarkers function was used with likelihood-ratio test for single cell gene expression. For heatmap representation, average expression of markers inside each cluster was used. To compare gene expression for the clusters inside cohorts (e.g., T cells, macrophages) we used FindMarkers function to calculate average log2 fold change and identify differentially expressed genes between each pair of experimental conditions using a Wilcoxon Rank-Sum test for calculating p-values and Bonferroni correction for adjusted p-values. Gene set enrichment analysis was performed using the fgsea package (version 1.32.0) to assess the enrichment of Hallmark gene sets from the Molecular Signatures Database (MSigDB). Hallmark gene sets were obtained using the msigdbr package (version 7.5.1). Differential gene expression analysis was performed using the FindMarkers function in Seurat (version 5.1.0) with the following parameters: threshold of log2 fold change = 0.2, and minimum percentage of expression = 0.1. Genes were ranked according to their log2 fold change, and these rankings were used as input for the enrichment analysis using the fgsea package.

Comparison to published datasets

The gene lists defining phenotype of intratumoral T cells were retrieved from published human or mouse scRNAseq datasets[34,42,44,45,69,90] (**Tables S2-S5**) to compare the cluster annotation between published study and our current study. The module scores for individual cells were

calculated using the “AddModuleScore” function in the Seurat package. The results were visualized using the normalized average module scores for each cluster (**Figs. 2H,** and **6C**).

Analysis of Bhlhe40 Regulon Activity

Single-Cell Regulatory Network Inference and Clustering (SCENIC) (version 1.3.1)[91] was performed with default parameters to explore transcriptional factor (TF) regulatory networks. Murine mm10 TF annotations were used as a reference, and co-expression modules between TFs and candidate target genes were inferred using GENIE3. Using the RcisTarget package (version 1.20.0), TF binding motifs enriched in the target gene sets were identified. Cell-type specific regulators were identified based on the Regulon Specificity Score (RSS)[92].

Trajectory analysis

Trajectory analysis was performed using the Monocle3 package (version 1.3.7)[93]. The Seurat object was converted into the Monocle3 object using the "as.cell_data_set" function. Cluster identities, dimensional reduction, and UMAP coordinates were transferred from Seurat object into the Monocle3 object. The trajectory was inferred with the default parameters.

Analysis of human datasets

The human scRNAseq data were collected from previously published datasets. Read count matrix was downloaded and metadata generated in Yost et al manuscript[76] (GSE123813). For Bassez et al[77] read count matrix and metadata are downloaded through VIB-Ku LEUVEN center for cancer biology (https://lambrechtslab.sites.vib.be/en/single-cell). Read count matrix from Sade-Feldman et al.[42] dataset was downloaded through GSE120575. Seurat objects then were generated and processed with Seurat pipeline. Seurat object of CD8 T cells in the paper from Minowa et al.[90] (GSE242477) were download from Zenodo (https://doi.org/10.5281/zenodo.12761836). For volcano plot from Oliveira et al[34], DEG list provided in the Oliveira et al. paper were used (phs001451.v3.p1). For volcano plot from Minowa et al, DEGs were identified by using FindMarkers function. For cell-type specific co-

expression, inference from scRNAseq data, CS-CORE package was utilized to create the co-expression heatmap[94].

Ex Vivo T Cell Stimulation

For PMA/ionomycin T cell stimulation, cells from tumors were enriched for CD8 T cells using Miltenyi mouse $CD8^+$ T cell enrichment from TIL kit by following manufacturer's protocol. Cells were then incubated with 10 ng/ml of PMA and 1 μg/ml of ionomycin in the presence of BD GolgiPlug (BD Bioscience) for 6 hours at 37 °C. and stained for IFN-γ and TNFα.

Adoptive Transfer and OT-I CD8 T cell Acute and Chronic Stimulation Assay

For adoptive transfer of OT-I CD8 T cells (transgenic for a TCR recognizing the H2-K^b-presented SIINFEKL epitope of OVA) into mice bearing B16-OVA melanoma, splenic CD8 T cells from $B^{+/+}$ OT-I and $B^{-/-}$ OT-I mice were stimulated with 1 nM of SIINFEKL peptide and intravenously transferred (4 x 10^6 cells per mouse). For acute and chronic antigen stimulation, naïve OT-I CD8 T cells from $B^{+/+}$ OT-I and $B^{-/-}$ OT-I mice were cocultured with naïve splenocytes pulsed with 1 nM of SIINFELK peptide. Chronic antigen stimulation was done to OT-I CD8 T cells by stimulating cells every 2 days with SIINFEKL peptide (1 nM) and rIL-2. Cells were harvested on day 10 post-first stimulation and processed for RT-qPCR.

Tetramer staining

Mutant Psmd6-H2-K^b-PE tetramers (IAPYYEAL) were obtained from the Baylor College of Medicine MHC Tetramer Production Facility. Cells were incubated at room temperature for 5 minutes with 500ng of rat anti-mouse anti-CD16/32 (mouse Fc block; clone 2.4G2, BD Biosciences) at 1μg/million cells. Peptide-H2-K^b tetramers conjugated with PE for mutated Psmd6 (1:500 dilution) were added to the cells and incubated for 20 minutes at 37^oC. Cells were further stained with an antibody mixture cocktail: anti-mouse CD45 BV605 (clone 30-F11) BioLegend (1:800 dilution), anti-mouse Thy1.2-PE-Cy7 (clone 30-H12) BioLegend (1:500 dilution), anti-mouse CD4-BV711 (clone RM4-5) (1:200 dilution) BioLegend, anti-mouse

CD8a-BV786 (clone 53-6.7) BioLegend (1:200 dilution), and live/dead (Zombie NIR) in 100 µl FACS buffer for 20 minutes at 4°C.

Flow cytometry

For flow cytometry, cells were stained for 5 minutes at room temperature with Fc block (anti-CD16/32) clone 2.4G2 (BD Bioscience) at 1 µg/million cells and then surfaced stained for 20 minutes at 4 °C. Surface antibodies were diluted in FACS staining buffer (PBS with 2% FCS, 2 mM EDTA, and 0.05% NaN_3 (Sigma)). Anti-mouse CD45 BV605 (clone 30-F11) BioLegend (1:800 dilution), anti-mouse CD3e-APC (clone 145-2C11) BioLegend (1:200 dilution), anti-mouse CD4-BV711 (clone RM4-5) (1:200 dilution) BioLegend, anti-mouse CD8a-BV786 (clone 53-6.7) BioLegend (1:200 dilution), anti-mouse CX3CR1-FITC (clone SA011F11) BioLegend (1:1000), anti-mouse I-A/I-E-BV650 (clone M5/114.15.2) BioLegend (1:3000 dilution), anti-mouse CD24-BV711 (clone M1/69) BD Bioscience, anti-mouse CD11c-BV786 (clone HL3) BD Bioscience (1:400 dilution), anti-mouse F4/80-BUV395 (clone T45-2342) BD Bioscience (1:400 dilution), anti-mouse CD64-BV421 (clone X54-5/7.1) BioLegend (1:400 dilution), anti-mouse Ly6G-Alexa Fluor 700 (clone 1A8) BD Bioscience (1:400 dilution), and anti-mouse CD11b-APC (clone M1/70) BioLegend (1:400 dilution) were used for surface stain at indicated dilutions. Zombie NIR Viability dye (BioLegend) was added at 1:500 during surface stain. For intracellular staining, surface-stained cells were fixed and permeabilized with BD fixation and permeabilization kit (BD Biosciences). Fixed and permeabilized cells were then stained with anti-mouse Mrc1 (CD206)-APC-Cy7 (clone C068C2) BioLegend (1:400 dilution) and anti-mouse iNOS/Nos2-PE (clone CXNFT) Thermo Fisher (1:400 dilution) for 30 minutes at 4 °C. For intracellular cytokine staining of lymphocytes, cells were isolated and then incubated at 37 °C for 6 hours with GolgiStop (BD Bioscience). Cells were then harvested, washed, stained for 5 minutes at room temperature with Fc block (anti-CD16/32) clone 2.4G2 (BD Bioscience) at 1 µg/million cells and then surfaced stained for 20 minutes at 4°C, and then fixed and permeabilized with BD fixation and permeabilization kit (BD Biosciences). Fixed and

permeabilized cells were then stained with anti-IFN-γ-APC (XMG1.2) BioLegend (1:200 dilution) and anti-TNF-α-PE-Cy7 (clone MP6-XT22) BioLegend (1:200 dilution) for 30 minutes at 4°C. All flow cytometry was performed on the LSR Fortessa X-20 (BD Biosciences) and analyzed using FlowJo software (TreeStar).

Fluorescence-activated cell sorting

For sorting of CD8/CD4 T cells and CD45.2^{+}Thy1.2^{+} cells, intratumoral cells were stained for 5 minutes at room temperature with Fc block (anti-CD16/32) clone 2.4G2 (BD Bioscience) at 1 μg/million cells and then were stained with surface antibodies against CD45, CD90.2/Thy1.2, CD8a, and CD4 for CD4/CD8 sorting and with CD45.2-PE (clone 104) BioLegend (1:1000 dilution) and CD90.2/Thy1.2 for CD45.2^{+}Thy1.2^{+} sorting along with Zombie NIR Viability dye and incubated for 30 minutes at 4°C. Cells were washed twice with MACS buffer and sorted gating on live CD45^{+}, CD90.2/Thy1.2^{+}, CD8a^{+}, CD4^{+} or CD45.2^{+},Thy1.2^{+}. Sorting was performed on a BD FACSAria II (BD Biosciences). CD8/CD4 sorted cells were processed for qPCR or CUT&RUN experiment and CD45.2^{+}Thy1.2^{+} sorted cells were processed for scRNA sequencing. The purity of the sorted cells for scRNAseq was greater than 97% as assessed during post-sort cellular analysis.

Magnetic cell sorting

Miltenyi Biotec's magnetic cell separation was used to isolate intratumoral CD8 T cells for Seahorse real-time ATP rate assay. Single cell suspension from tumors were resuspended in MACS buffer, along with 10 μl of CD8 (TIL) microbeads per 10^{7} total cells and incubated for 15 minutes in 4°C. After incubation, CD8 T cell fractions were isolated in a magnetic field using MACS separator according to the manufacturer's protocol. Isolated CD8 T cells were processed for Seahorse real-time ATP rate assay.

Seahorse XF Real-Time ATP Rate Assay

The Seahorse XF Real-Time ATP Rate Assay (Agilent, 103592-100) were performed on a Seahorse XFe96 Analyzer (Agilent) according to the manufacturer's protocol. Briefly, 1 × 10 cells/well were seeded in Seahorse XF RPMI-1640 medium (Agilent, 103576-100) supplemented with 1 mM pyruvate (103578-100), 10 mM glucose (103577-100), and 2 mM glutamine (103579-100) in a Cell-Tak–coated Seahorse XF96 cell culture microplate. Cells were centrifuged at 200 × g for 1 minute (no brake) and then incubated in a 37°C non-CO incubator for 30 minutes to allow complete adherence. Pre-hydrated sensor cartridges were loaded with 1.5 µM oligomycin and 0.5 µM rotenone/antimycin, which were sequentially injected during the assay to measure oxygen consumption rate (OCR) and extracellular acidification rate (ECAR) in real time. Data were analyzed using Wave Software (Agilent, v2.6.3.5) to calculate ATP production rates derived from mitochondrial oxidative phosphorylation (OXPHOS) and glycolysis, and values were normalized to seeded cell numbers.

Cleavage Under Targets and Release Using Nuclease (CUT&RUN) Assay: CUT&RUN was performed at the MD Anderson Cancer Center Epigenomics Profiling Core following the protocol as described[95,96] with some modifications. Briefly, nuclei isolated from ~500,000 live intratumoral CD8 T cells were immobilized on Concanavalin A-coated magnetic beads (Bangs Laboratories) and permeabilized using wash buffer containing 0.02% digitonin (Promega). Bead-bound nuclei were incubated with rabbit IgG (Millipore) and Bhlhe40 (NB100-1800 EpiCypher) antibodies overnight at 4°C. Next day, targeted chromatin digestion was achieved by pAG-MNase (EpiCypher) binding for 10min at room temperature followed by incubation with $CaCl_2$ at 4°C. CUT&RUN DNA was purified using MinElute columns (Qiagen). Library preparation was carried out using the NEBNext® Ultra™ II DNA Library Prep Kit for Illumina® (New England Biolabs) according to the manufacturer's instructions with some modifications, and sequencing was performed on an Illumina NovaSeq platform to obtain ~10 million reads per sample.

CUT&RUN analysis

Raw sequencing reads were quality-checked using FastQC (v0.12.1). Adapter sequences and low-quality bases were removed using fastp (v0.24.0) with automatic adapter detection for paired-end reads based on per-read overlap analysis. Clean reads were aligned to the mouse reference genome (GRCm38/mm10) using Bowtie2 (v2.5.4) with parameters -I 25 -X 1000 --no-mixed --no-discordant --very-sensitive. Aligned reads were sorted and indexed using SAMtools (v1.21). Mitochondrial reads, unmapped reads, multi-mapped reads, and reads with mapping quality <30 were removed. PCR duplicates were marked using Picard (v3.4.0). Genome-wide coverage tracks (BigWig and BedGraph) were generated using deepTools (v3.5.6) bamCoverage. Peaks were called using MACS2 (v2.2.6; $p < 1 \times 10^{\square\square}$). Differential binding analysis was performed using MAnorm (v3.16.0), and peaks with MA values >1 or <−1 ($p < 0.05$) were considered differential. Peaks were annotated to the nearest genes using ChIPseeker (v1.42.0).

Statistical analysis

Samples were compared using an unpaired, two-tailed Student's *t*-test, two-way ANOVA, or log-rank (Mantel-Cox) test unless specified otherwise.

Data and Software Availability

Raw sequence files (accession number: PRJNA1426211) and processed data files for the scRNAseq reported in this paper is deposited in the Gene Expression Omnibus (GEO) database (GEO accession number: GSE320057) and made publicly available at the time of publication. Software used in this study is available online: current version of Cell Ranger: https://support.10xgenomics.com/single-cell-gene-expression/software/downloads/latest; Seurat 4.0: https://satijalab.org/seurat/; ggplot2 3.3.3: https://ggplot2.tidyverse.org/index.html; and ImmGen: https://www.immgen.org.

Author's Contributions

Conceptualization, A.S., T.M, A.S.S., and M.M.G.; data curation, A.S., T.M., A.S.S., A.J.S., S.K., and M.M.G.; investigation, A.S., T.M., A.S.S., S.K., N.N.J., and M.M.G.; visualization, A.S., T.M., A.S.S., S.K., M.M.G.; methodology, A.S., T.M., and M.M.G.; data analysis, A.S., T.M., A.S.S., N.N.J., S.S., A.K.J., and K.R.; formal analysis, A.S., N.N.J., K.E.P., K.H.H., B.T.E., K.C., and M.M.G.; validation, A.S. and M.M.G.; writing – original draft, A.S. and M.M.G.; writing – review & editing, A.S., T.M., K.E.P., K.H.H., B.T.E., K.C., A.K.J., and M.M.G.; resources, B.T.E., K.C., and M.M.G.; supervision, M.M.G.; project administration, M.M.G.

Acknowledgments

M.M.G. was a Cancer Prevention and Research Institute of Texas (CPRIT) Scholar in Cancer Research and an Andrew Sabin Family Foundation Fellow during part of this study. This work was supported by CPRIT (Recruitment of First-Time Tenure-Track Faculty Members; RR190017), an Andrew Sabin Family Foundation Fellowship, a Parker Institute for Cancer Immunotherapy (PICI) Bridge Scholar Award, a University of Texas (UT) Rising Stars Award, and NCI R01CA282027 to M.M.G. and NCI U01CA247760 to K.C. K.H.H. is a CPRIT Scholar in Cancer Research and a PICI and V Foundation Bridge Scholar. K.E.P. was supported by an Andrew Sabin Family Foundation Fellowship at MD Anderson Cancer Center (MDACC), a Melanoma SPORE Developmental Research Program grant at MDACC (grant P50CA221703 from NCI), and the UT Rising Stars Award. AKJ is partially supported by MDACC institutional funds to the Epigenomics Profiling Core. We thank MDACC Epigenomics Profiling Core (EpiCore) for assistance with CUT&RUN assays. The MDACC Flow Cytometry and Cellular Imaging Core Facility and the Advanced Technology Genomics Core (ATGC) are supported by NCI Core grant P30CA016672. We would like to thank David Pollock at ATGC for assistance with scRNA-seq. We would like to thank X. Lily Wang at Baylor College of Medicine MHC

Tetramer Core for production of tetramers used in this study. We would like to thank Waikin Chan at MDACC Metabolomics core for assistance with real-time ATP assays.

Declaration of interests

K.R. reports equity in Jivanu Therapeutics and Koshika Therapeutics, research funding from Cyclacel, and a consulting fee from Daiichi Sankyo that is unrelated to the current work. K.E.P. reports a patent on T cell exhaustion state-specific gene expression regulators and uses thereof (US2021/0309965 A1) that is unrelated to the current work. M.M.G. reports a personal honorarium from Springer Nature Ltd for his role as a Deputy Editor for the journal Nature Precision Oncology and served as a paid consultant for Merck. No disclosures were reported by the other authors.

REFERENCES:

1 Leach, D. R., Krummel, M. F. & Allison, J. P. Enhancement of antitumor immunity by CTLA-4 blockade. *Science* **271**, 1734-1736 (1996). https://doi.org/10.1126/science.271.5256.1734

2 Kalbasi, A. & Ribas, A. Tumour-intrinsic resistance to immune checkpoint blockade. *Nat Rev Immunol* **20**, 25-39 (2020). https://doi.org/10.1038/s41577-019-0218-4

3 Sharma, P. *et al.* The Next Decade of Immune Checkpoint Therapy. *Cancer Discov* **11**, 838-857 (2021). https://doi.org/10.1158/2159-8290.CD-20-1680

4 Wolchok, J. D. *et al.* Long-Term Outcomes With Nivolumab Plus Ipilimumab or Nivolumab Alone Versus Ipilimumab in Patients With Advanced Melanoma. *J Clin Oncol* **40**, 127-137 (2022). https://doi.org/10.1200/JCO.21.02229

5 Gubin, M. M. & Vesely, M. D. Cancer Immunoediting in the Era of Immuno-oncology. *Clin Cancer Res* **28**, 3917-3928 (2022). https://doi.org/10.1158/1078-0432.CCR-21-1804

6 Sharma, P. *et al.* Immune checkpoint therapy-current perspectives and future directions. *Cell* **186**, 1652-1669 (2023). https://doi.org/10.1016/j.cell.2023.03.006

7 Wolchok, J. D. *et al.* Final, 10-Year Outcomes with Nivolumab plus Ipilimumab in Advanced Melanoma. *N Engl J Med* **392**, 11-22 (2025). https://doi.org/10.1056/NEJMoa2407417

8 Heemskerk, B., Kvistborg, P. & Schumacher, T. N. The cancer antigenome. *The EMBO journal* **32**, 194-203 (2013). https://doi.org/10.1038/emboj.2012.333

9 van Rooij, N. *et al.* Tumor exome analysis reveals neoantigen-specific T-cell reactivity in an ipilimumab-responsive melanoma. *J Clin Oncol* **31**, e439-442 (2013). https://doi.org/10.1200/JCO.2012.47.7521

10 Coulie, P. G., Van den Eynde, B. J., van der Bruggen, P. & Boon, T. Tumour antigens recognized by T lymphocytes: at the core of cancer immunotherapy. *Nat Rev Cancer* **14**, 135-146 (2014). https://doi.org/10.1038/nrc3670

11 Gubin, M. M. *et al.* Checkpoint blockade cancer immunotherapy targets tumour-specific mutant antigens. *Nature* **515**, 577-581 (2014). https://doi.org/10.1038/nature13988

12 Kreiter, S. *et al.* Mutant MHC class II epitopes drive therapeutic immune responses to cancer. *Nature* **520**, 692-696 (2015). https://doi.org/10.1038/nature14426

13 Schumacher, T. N. & Schreiber, R. D. Neoantigens in cancer immunotherapy. *Science* **348**, 69-74 (2015). https://doi.org/10.1126/science.aaa4971

14 Fehlings, M. *et al.* Checkpoint blockade immunotherapy reshapes the high-dimensional phenotypic heterogeneity of murine intratumoural neoantigen-specific CD8(+) T cells. *Nat Commun* **8**, 562 (2017). https://doi.org/10.1038/s41467-017-00627-z

15 Brightman, S. E., Naradikian, M. S., Miller, A. M. & Schoenberger, S. P. Harnessing neoantigen specific CD4 T cells for cancer immunotherapy. *J Leukoc Biol* **107**, 625-633 (2020). https://doi.org/10.1002/JLB.5RI0220-603RR

16 Cui, C. *et al.* Neoantigen-driven B cell and CD4 T follicular helper cell collaboration promotes anti-tumor CD8 T cell responses. *Cell* **184**, 6101-6118 e6113 (2021). https://doi.org/10.1016/j.cell.2021.11.007

17 Chen, Z. *et al.* TCF-1-Centered Transcriptional Network Drives an Effector versus Exhausted CD8 T Cell-Fate Decision. *Immunity* **51**, 840-855 e845 (2019). https://doi.org/10.1016/j.immuni.2019.09.013

18 Zheng, L. *et al.* Pan-cancer single-cell landscape of tumor-infiltrating T cells. *Science* **374**, abe6474 (2021). https://doi.org/10.1126/science.abe6474

19 Caushi, J. X. *et al.* Transcriptional programs of neoantigen-specific TIL in anti-PD-1-treated lung cancers. *Nature* **596**, 126-132 (2021). https://doi.org/10.1038/s41586-021-03752-4

20 Wei, S. C. *et al.* Distinct Cellular Mechanisms Underlie Anti-CTLA-4 and Anti-PD-1 Checkpoint Blockade. *Cell* **170**, 1120-1133 e1117 (2017). https://doi.org/10.1016/j.cell.2017.07.024

21 Gubin, M. M. *et al.* High-Dimensional Analysis Delineates Myeloid and Lymphoid Compartment Remodeling during Successful Immune-Checkpoint Cancer Therapy. *Cell* **175**, 1014-1030 e1019 (2018). https://doi.org/10.1016/j.cell.2018.09.030

22 Cook, M. E., Jarjour, N. N., Lin, C. C. & Edelson, B. T. Transcription Factor Bhlhe40 in Immunity and Autoimmunity. *Trends Immunol* **41**, 1023-1036 (2020). https://doi.org/10.1016/j.it.2020.09.002

23 Lin, C. C. *et al.* Bhlhe40 controls cytokine production by T cells and is essential for pathogenicity in autoimmune neuroinflammation. *Nat Commun* **5**, 3551 (2014). https://doi.org/10.1038/ncomms4551

24 Huynh, J. P. *et al.* Bhlhe40 is an essential repressor of IL-10 during Mycobacterium tuberculosis infection. *J Exp Med* **215**, 1823-1838 (2018). https://doi.org/10.1084/jem.20171704

25 Kanda, M. *et al.* Transcriptional regulator Bhlhe40 works as a cofactor of T-bet in the regulation of IFN-gamma production in iNKT cells. *Proc Natl Acad Sci U S A* **113**, E3394-3402 (2016). https://doi.org/10.1073/pnas.1604178113

26 Li, C. *et al.* The Transcription Factor Bhlhe40 Programs Mitochondrial Regulation of Resident CD8(+) T Cell Fitness and Functionality. *Immunity* **52**, 201-202 (2020). https://doi.org/10.1016/j.immuni.2019.12.008

27 Lin, C. C. *et al.* IL-1-induced Bhlhe40 identifies pathogenic T helper cells in a model of autoimmune neuroinflammation. *J Exp Med* **213**, 251-271 (2016). https://doi.org/10.1084/jem.20150568

28 Uyeda, M. J. *et al.* BHLHE40 Regulates IL-10 and IFN-gamma Production in T Cells but Does Not Interfere With Human Type 1 Regulatory T Cell Differentiation. *Front Immunol* **12**, 683680 (2021). https://doi.org/10.3389/fimmu.2021.683680

29 Martinez-Llordella, M. *et al.* CD28-inducible transcription factor DEC1 is required for efficient autoreactive CD4+ T cell response. *J Exp Med* **210**, 1603-1619 (2013). https://doi.org/10.1084/jem.20122387

30 Salmon, A. J. *et al.* BHLHE40 Regulates the T-Cell Effector Function Required for Tumor Microenvironment Remodeling and Immune Checkpoint Therapy Efficacy. *Cancer Immunol Res* **10**, 597-611 (2022). https://doi.org/10.1158/2326-6066.CIR-21-0129

31 Cook, M. E. *et al.* BHLHE40 Mediates Cross-Talk between Pathogenic TH17 Cells and Myeloid Cells during Experimental Autoimmune Encephalomyelitis. *Immunohorizons* **7**, 737-746 (2023). https://doi.org/10.4049/immunohorizons.2300042

32 Yu, F. *et al.* The transcription factor Bhlhe40 is a switch of inflammatory versus antiinflammatory Th1 cell fate determination. *J Exp Med* **215**, 1813-1821 (2018). https://doi.org/10.1084/jem.20170155

33 Meier, S. L., Satpathy, A. T. & Wells, D. K. Bystander T cells in cancer immunology and therapy. *Nat Cancer* **3**, 143-155 (2022). https://doi.org/10.1038/s43018-022-00335-8

34 Oliveira, G. *et al.* Phenotype, specificity and avidity of antitumour CD8(+) T cells in melanoma. *Nature* **596**, 119-125 (2021). https://doi.org/10.1038/s41586-021-03704-y

35 Lowery, F. J. *et al.* Molecular signatures of antitumor neoantigen-reactive T cells from metastatic human cancers. *Science* **375**, 877-884 (2022). https://doi.org/10.1126/science.abl5447

36 Lee, P. P. *et al.* A critical role for Dnmt1 and DNA methylation in T cell development, function, and survival. *Immunity* **15**, 763-774 (2001). https://doi.org/10.1016/s1074-7613(01)00227-8

37 Maekawa, Y. *et al.* Notch2 integrates signaling by the transcription factors RBP-J and CREB1 to promote T cell cytotoxicity. *Nat Immunol* **9**, 1140-1147 (2008). https://doi.org/10.1038/ni.1649

38 Meng, W. *et al.* Improvement of Tumor Neoantigen Detection by High-Field Asymmetric Waveform Ion Mobility Mass Spectrometry. *Cancer Immunol Res* **12**, 988-1006 (2024). https://doi.org/10.1158/2326-6066.CIR-23-0900

39 Sultan, H. *et al.* Neoantigen-specific cytotoxic Tr1 CD4 T cells suppress cancer immunotherapy. *Nature* **632**, 182-191 (2024). https://doi.org/10.1038/s41586-024-07752-y

40 Meeth, K., Wang, J. X., Micevic, G., Damsky, W. & Bosenberg, M. W. The YUMM lines: a series of congenic mouse melanoma cell lines with defined genetic alterations. *Pigment Cell Melanoma Res* **29**, 590-597 (2016). https://doi.org/10.1111/pcmr.12498

41 Keshari, S. *et al.* Comparing neoantigen cancer vaccines and immune checkpoint therapy unveils an effective vaccine and anti-TREM2 macrophage-targeting dual therapy. *Cell Rep* **43**, 114875 (2024). https://doi.org/10.1016/j.celrep.2024.114875

42 Sade-Feldman, M. *et al.* Defining T Cell States Associated with Response to Checkpoint Immunotherapy in Melanoma. *Cell* **175**, 998-1013 e1020 (2018). https://doi.org/10.1016/j.cell.2018.10.038

43 Miller, B. C. *et al.* Subsets of exhausted CD8(+) T cells differentially mediate tumor control and respond to checkpoint blockade. *Nat Immunol* **20**, 326-336 (2019). https://doi.org/10.1038/s41590-019-0312-6

44 Pauken, K. E. *et al.* Single-cell analyses identify circulating anti-tumor CD8 T cells and markers for their enrichment. *J Exp Med* **218** (2021). https://doi.org/10.1084/jem.20200920

45 Chu, Y. *et al.* Pan-cancer T cell atlas links a cellular stress response state to immunotherapy resistance. *Nat Med* **29**, 1550-1562 (2023). https://doi.org/10.1038/s41591-023-02371-y

46 Barber, D. L. *et al.* Restoring function in exhausted CD8 T cells during chronic viral infection. *Nature* **439**, 682-687 (2006). https://doi.org/10.1038/nature04444

47 Pauken, K. E. *et al.* Epigenetic stability of exhausted T cells limits durability of reinvigoration by PD-1 blockade. *Science* **354**, 1160-1165 (2016). https://doi.org/10.1126/science.aaf2807

48 Blank, C. U. *et al.* Defining 'T cell exhaustion'. *Nat Rev Immunol* **19**, 665-674 (2019). https://doi.org/10.1038/s41577-019-0221-9

49 Belk, J. A. *et al.* Genome-wide CRISPR screens of T cell exhaustion identify chromatin remodeling factors that limit T cell persistence. *Cancer Cell* **40**, 768-786 e767 (2022). https://doi.org/10.1016/j.ccell.2022.06.001

50 Giles, J. R., Globig, A. M., Kaech, S. M. & Wherry, E. J. CD8(+) T cells in the cancer-immunity cycle. *Immunity* **56**, 2231-2253 (2023). https://doi.org/10.1016/j.immuni.2023.09.005

51 Jennings, E. *et al.* Nr4a1 and Nr4a3 Reporter Mice Are Differentially Sensitive to T Cell Receptor Signal Strength and Duration. *Cell Rep* **33**, 108328 (2020). https://doi.org/10.1016/j.celrep.2020.108328

52 Hao, J. *et al.* NR4A1 transcriptionally regulates the differentiation of stem-like CD8(+) T cells in the tumor microenvironment. *Cell Rep* **43**, 114301 (2024). https://doi.org/10.1016/j.celrep.2024.114301

53 Scott, A. C. *et al.* TOX is a critical regulator of tumour-specific T cell differentiation. *Nature* **571**, 270-274 (2019). https://doi.org/10.1038/s41586-019-1324-y

54 Khan, O. *et al.* TOX transcriptionally and epigenetically programs CD8(+) T cell exhaustion. *Nature* **571**, 211-218 (2019). https://doi.org/10.1038/s41586-019-1325-x

55 Alfei, F. *et al.* TOX reinforces the phenotype and longevity of exhausted T cells in chronic viral infection. *Nature* **571**, 265-269 (2019). https://doi.org/10.1038/s41586-019-1326-9

56 Philip, M. & Schietinger, A. CD8(+) T cell differentiation and dysfunction in cancer. *Nat Rev Immunol* **22**, 209-223 (2022). https://doi.org/10.1038/s41577-021-00574-3

57 Utzschneider, D. T. *et al.* T Cell Factor 1-Expressing Memory-like CD8(+) T Cells Sustain the Immune Response to Chronic Viral Infections. *Immunity* **45**, 415-427 (2016). https://doi.org/10.1016/j.immuni.2016.07.021

58 Siddiqui, I. *et al.* Intratumoral Tcf1(+)PD-1(+)CD8(+) T Cells with Stem-like Properties Promote Tumor Control in Response to Vaccination and Checkpoint Blockade Immunotherapy. *Immunity* **50**, 195-211 e110 (2019). https://doi.org/10.1016/j.immuni.2018.12.021

59 Escobar, G., Mangani, D. & Anderson, A. C. T cell factor 1: A master regulator of the T cell response in disease. *Sci Immunol* **5** (2020). https://doi.org/10.1126/sciimmunol.abb9726

60 Gill, A. L. *et al.* PD-1 blockade increases the self-renewal of stem-like CD8 T cells to compensate for their accelerated differentiation into effectors. *Sci Immunol* **8**, eadg0539 (2023). https://doi.org/10.1126/sciimmunol.adg0539

61 Wang, K. *et al.* Combination anti-PD-1 and anti-CTLA-4 therapy generates waves of clonal responses that include progenitor-exhausted CD8(+) T cells. *Cancer Cell* **42**, 1582-1597 e1510 (2024). https://doi.org/10.1016/j.ccell.2024.08.007

62 Mok, S. *et al.* Anti-CTLA-4 generates greater memory response than anti-PD-1 via TCF-1. *Proc Natl Acad Sci U S A* **122**, e2418985122 (2025). https://doi.org/10.1073/pnas.2418985122

63 Kovanen, P. E. *et al.* T-cell development and function are modulated by dual specificity phosphatase DUSP5. *J Biol Chem* **283**, 17362-17369 (2008). https://doi.org/10.1074/jbc.M709887200

64 Kutty, R. G. *et al.* Dual Specificity Phosphatase 5 Is Essential for T Cell Survival. *PLoS One* **11**, e0167246 (2016). https://doi.org/10.1371/journal.pone.0167246

65 Zhou, P. *et al.* Single-cell CRISPR screens in vivo map T cell fate regulomes in cancer. *Nature* **624**, 154-163 (2023). https://doi.org/10.1038/s41586-023-06733-x

66 Yao, C. *et al.* BACH2 enforces the transcriptional and epigenetic programs of stem-like CD8(+) T cells. *Nat Immunol* **22**, 370-380 (2021). https://doi.org/10.1038/s41590-021-00868-7

67 Zhong, Y. *et al.* Hierarchical regulation of the resting and activated T cell epigenome by major transcription factor families. *Nat Immunol* **23**, 122-134 (2022). https://doi.org/10.1038/s41590-021-01086-x

68 Simpson, T. R. *et al.* Fc-dependent depletion of tumor-infiltrating regulatory T cells co-defines the efficacy of anti-CTLA-4 therapy against melanoma. *J Exp Med* **210**, 1695-1710 (2013). https://doi.org/10.1084/jem.20130579

69 Oliveira, G. *et al.* Landscape of helper and regulatory antitumour CD4(+) T cells in melanoma. *Nature* **605**, 532-538 (2022). https://doi.org/10.1038/s41586-022-04682-5

70 Liakou, C. I. *et al.* CTLA-4 blockade increases IFNgamma-producing CD4+ICOShi cells to shift the ratio of effector to regulatory T cells in cancer patients. *Proc Natl Acad Sci U S A* **105**, 14987-14992 (2008). https://doi.org/10.1073/pnas.0806075105

71 Chen, H. *et al.* Anti-CTLA-4 therapy results in higher CD4+ICOShi T cell frequency and IFN-gamma levels in both nonmalignant and malignant prostate tissues. *Proc Natl Acad Sci U S A* **106**, 2729-2734 (2009). https://doi.org/10.1073/pnas.0813175106

72 Ng Tang, D. *et al.* Increased frequency of ICOS+ CD4 T cells as a pharmacodynamic biomarker for anti-CTLA-4 therapy. *Cancer Immunol Res* **1**, 229-234 (2013). https://doi.org/10.1158/2326-6066.CIR-13-0020

73 Salmon, A. J. *et al.* BHLHE40 Regulates the T-Cell Effector Function Required for Tumor Microenvironment Remodeling and Immune Checkpoint-Therapy Efficacy. *Cancer Immunol Res* (2022). https://doi.org/10.1158/2326-6066.CIR-21-0129

74 Molgora, M. *et al.* TREM2 Modulation Remodels the Tumor Myeloid Landscape Enhancing Anti-PD-1 Immunotherapy. *Cell* **182**, 886-900 e817 (2020). https://doi.org/10.1016/j.cell.2020.07.013

75 Katzenelenbogen, Y. *et al.* Coupled scRNA-Seq and Intracellular Protein Activity Reveal an Immunosuppressive Role of TREM2 in Cancer. *Cell* **182**, 872-885 e819 (2020). https://doi.org/10.1016/j.cell.2020.06.032

76 Yost, K. E. *et al.* Clonal replacement of tumor-specific T cells following PD-1 blockade. *Nat Med* **25**, 1251-1259 (2019). https://doi.org/10.1038/s41591-019-0522-3

77 Bassez, A. *et al.* A single-cell map of intratumoral changes during anti-PD1 treatment of patients with breast cancer. *Nat Med* **27**, 820-832 (2021). https://doi.org/10.1038/s41591-021-01323-8

78 Verma, A. *et al.* TCF1 dosage determines cell fate during T cell development. *Sci Adv* **10**, eado5982 (2024). https://doi.org/10.1126/sciadv.ado5982

79 Wu, J. E. *et al.* In vitro modeling of CD8(+) T cell exhaustion enables CRISPR screening to reveal a role for BHLHE40. *Sci Immunol* **8**, eade3369 (2023). https://doi.org/10.1126/sciimmunol.ade3369

80 Blackburn, S. D., Shin, H., Freeman, G. J. & Wherry, E. J. Selective expansion of a subset of exhausted CD8 T cells by alphaPD-L1 blockade. *Proc Natl Acad Sci U S A* **105**, 15016-15021 (2008). https://doi.org/10.1073/pnas.0801497105

81 Im, S. J. *et al.* Defining CD8+ T cells that provide the proliferative burst after PD-1 therapy. *Nature* **537**, 417-421 (2016). https://doi.org/10.1038/nature19330

82 Nguyen, C. *et al.* Bhlhe40 Promotes CD4+ T Helper 1 Cell and Suppresses T Follicular Helper Cell Differentiation during Viral Infection. *J Immunol* **212**, 1829-1842 (2024). https://doi.org/10.4049/jimmunol.2300355

83 Chang, C. H. *et al.* Metabolic Competition in the Tumor Microenvironment Is a Driver of Cancer Progression. *Cell* **162**, 1229-1241 (2015). https://doi.org/10.1016/j.cell.2015.08.016

84 Siska, P. J. & Rathmell, J. C. T cell metabolic fitness in antitumor immunity. *Trends Immunol* **36**, 257-264 (2015). https://doi.org/10.1016/j.it.2015.02.007

85 Geltink, R. I. K., Kyle, R. L. & Pearce, E. L. Unraveling the Complex Interplay Between T Cell Metabolism and Function. *Annu Rev Immunol* **36**, 461-488 (2018). https://doi.org/10.1146/annurev-immunol-042617-053019

86 Wilfahrt, D. & Delgoffe, G. M. Metabolic waypoints during T cell differentiation. *Nat Immunol* **25**, 206-217 (2024). https://doi.org/10.1038/s41590-023-01733-5

87 Delgoffe, G. M. & Powell, J. D. Feeding an army: The metabolism of T cells in activation, anergy, and exhaustion. *Mol Immunol* **68**, 492-496 (2015). https://doi.org/10.1016/j.molimm.2015.07.026

88 Sun, H., Lu, B., Li, R. Q., Flavell, R. A. & Taneja, R. Defective T cell activation and autoimmune disorder in Stra13-deficient mice. *Nat Immunol* **2**, 1040-1047 (2001). https://doi.org/10.1038/ni721

89 Shankaran, V. *et al.* IFNgamma and lymphocytes prevent primary tumour development and shape tumour immunogenicity. *Nature* **410**, 1107-1111 (2001). https://doi.org/10.1038/35074122

90 Minowa, T. *et al.* Single-cell profiling of acral melanoma infiltrating lymphocytes reveals a suppressive tumor microenvironment. *Sci Transl Med* **16**, eadk8832 (2024). https://doi.org/10.1126/scitranslmed.adk8832

91 Aibar, S. *et al.* SCENIC: single-cell regulatory network inference and clustering. *Nat Methods* **14**, 1083-1086 (2017). https://doi.org/10.1038/nmeth.4463

92 Suo, S. *et al.* Revealing the Critical Regulators of Cell Identity in the Mouse Cell Atlas. *Cell Rep* **25**, 1436-1445 e1433 (2018). https://doi.org/10.1016/j.celrep.2018.10.045

93 Cao, J. *et al.* The single-cell transcriptional landscape of mammalian organogenesis. *Nature* **566**, 496-502 (2019). https://doi.org/10.1038/s41586-019-0969-x

94 Su, C. *et al.* Cell-type-specific co-expression inference from single cell RNA-sequencing data. *Nat Commun* **14**, 4846 (2023). https://doi.org/10.1038/s41467-023-40503-7

95 Meers, M. P., Bryson, T. D., Henikoff, J. G. & Henikoff, S. Improved CUT&RUN chromatin profiling tools. *Elife* **8** (2019). https://doi.org/10.7554/eLife.46314

96 Chen, Y. C., Bhaskara, G. B., Lu, Y., Lin, K. & Dent, S. Y. R. The SAGA acetyltransferase module is required for the maintenance of MAF and MYC oncogenic gene expression programs in multiple myeloma. *Genes Dev* **38**, 738-754 (2024). https://doi.org/10.1101/gad.351789.124

FIGURE LEGENDS:

Figure 1. Bhlhe40 is expressed in tumor-reactive human T cells. (A) *BHLHE40* transcript levels across immune cell types and various tumor types from The Cancer Genome Atlas (TCGA) datasets analyzed via GEPIA2021 (https://doi.org/10.1093/nar/gkab418). **(B)** Differential gene expression analysis comparing tumor-reactive CD8 T cells with non-tumor-specific or non-reactive CD8 T cells (as defined by Oliveira et al. and Minowa et al.) in cutaneous and acral melanoma.

Figure 2. CD8 T cell-intrinsic Bhlhe40 is essential for anti-PD-1 but not anti-CTLA-4 efficacy. (A) Bhlhe40 conditional knockout mice bearing 1956 MCA sarcoma were treated with anti-PD-1 or anti-CTLA-4 as indicated. **(B)** Tumor growth and percent tumor rejection of 1956 tumors in Bhlhe40$^{fl/fl}$ (B$^{f/f}$) and Bhlhe40$^{\Delta CD8}$ (B$^{\Delta CD8}$) mice treated with control antibody (Ab), anti-PD-1, or anti-CTLA-4. **(C)** UMAP generated from integration of CD8 T cells from scRNAseq Experiment #1 and scRNAseq Experiment #2 depicting CD8 T cell clusters named based on phenotypic markers. **(D)** Feature plots displaying expression of select markers. **(E)** Violin plots showing *Bhlhe40* expression in CD8 T cells by cluster and treatment in B$^{f/f}$ mice. **(F)** Dot plot showing the regulon specificity score across transcription factors. The top five regulons and Bhlhe40 in PD1^{hi}_Eff_Ex cluster are highlighted in red and labeled on the plot. **(G)** Heatmaps comparing features (module scores) of CD8 T cell clusters (rows) to published mouse and human CD8 T cell gene signatures (columns) identified/annotated by Miller et al. and Pauken et al. (mouse) and by Chu et al., Oliveira et al., and Sade-Feldman et al. (human). For (**B**), tumor growth is presented as mean +/- SEM of mean tumor diameter of individual mice and are representative of at least three independent experiments (∗∗∗$p < 0.001$; ns, not significant, 2-way ANOVA). Tumor rejection graphs display cumulative percentage of mice with complete tumor rejection from 3-4 independent experiments.

Figure 3. Bhlhe40 regulates NeoAg-specific CD8 T cell responses to anti-PD-1 and supports IFN-γ production. (A) Bar graph showing percent of CD8 T cells as determined by flow cytometry staining of intratumoral cells isolated from 1956 tumor-bearing $B^{f/f}$ and $B^{\Delta CD8}$ mice treated with control Ab, anti-PD-1, or anti-CTLA-4. **(B)** Flow cytometry plots of mPsmd6 peptide-H2-K^b tetramer staining for NeoAg-specific CD8 T cells in $B^{f/f}$ and $B^{\Delta CD8}$ mice treated with control Ab, anti-PD-1, or anti-CTLA-4. Gated on live CD8 T cells. **(C)** Graphs displaying IFN-γ^+ CD8 T cells (as a percentage of CD8 T cells), IFN-γ MFI of IFN-γ^+ CD8 T cells, and IFN-γ^+ TNF-α^+ CD8 T cells (as a percentage of CD8 T cells). **(D)** Heatmap displaying normalized Hallmark IFNγ response GSEA enrichment score (NES) for CD8 T cell clusters in $B^{\Delta CD8}$ versus $B^{f/f}$ mice treated with anti-PD-1 or anti-CTLA-4. **(E)** GSEA plots for the Hallmark IFNγ response in $PD1^{hi}$_Eff_Ex, $Nr4a1^{hi}$_Eff_Ex and Eff_Cycling CD8 T cell clusters in $B^{\Delta CD8}$ mice comparing anti-CTLA-4 vs anti-PD-1 treatment. For Bar graphs in (**A**) display the mean ± SEM and are representative of at least three independent experiments (∗∗$p < 0.01$; ns, not significant, unpaired t test). For (**C**), IFN-γ and TNF-α was determined via intracellular cytokine staining of *ex vivo* restimulated CD8 T cells isolated from 1956 tumors on day 10 post-tumor transplant. Bar graphs display the mean ± SEM and are representative of at least three independent experiments (∗∗$p < 0.01$, ∗∗∗$p < 0.001$; ns, not significant, unpaired t test).

Figure 4. CD8 T cell-intrinsic Bhlhe40 governs effector differentiation. (A) Spearman correlation analysis of all CD8 T cell clusters relative to Bhlhe40 compared in $B^{f/f}$ mice. Dot color indicates the p-value. **(B)** UMAP of CD8 T cells showing the Monocle3 trajectory across all samples, colored by inferred pseudotime. **(C)** Pseudo-temporal trends of *Bhlhe40* and *Tcf7* in CD8 T cells from $B^{f/f}$ mice. **(D)** Graphs displaying PD-1^+TCF-1^+ CD8 T cells (as a percentage of CD8 T cells). **(E)** Genome track plots showing Bhlhe40 CUT&RUN peaks at *Tcf7* locus in intratumoral CD8 T cells isolated from WT mice treated with control Ab, anti-PD-1, or anti-CTLA-4. **(F)** Genome track plots showing Bhlhe40 CUT&RUN peaks at *Bach2* locus in

intratumoral CD8 T cells isolated from WT mice treated with control Ab, anti-PD-1, or anti-CTLA-4. **(G)** Tumor growth of B16-OVA tumors in mice adoptively transferred with either PBS, Bhlhe40$^{+/+}$ ($B^{+/+}$) OT-I or Bhlhe40$^{-/-}$ ($B^{-/-}$) OT-I splenocytes stimulated ex vivo with SIINFEKL peptide. **(H)** Heatmap displaying transcript expression of effector/exhaustion markers (*Pdcd1, Lag3, Havcr2, Ifng*) and memory-associated markers (*Tcf7, Il7r*) in $B^{+/+}$ and $B^{-/-}$ OT-I T cells under ex vivo acute and chronic stimulation conditions with cognate SIINFEKL peptide-loaded APCs. For (**D**), TCF-1 and PD-1 expression was assessed via intracellular/intranuclear staining and flow cytometry of 1956 tumors on day 10 post-tumor transplant. Bar graphs display the mean ± SEM and are representative of two independent experiments (∗$p < 0.05$; ∗∗$p < 0.01$, ns, not significant, unpaired t test). Tumor growth in (**G**) is presented as mean +/- SEM of mean tumor diameter of individual mice and is representative of two independent experiments (∗∗∗$p < 0.001$; ∗∗∗∗$p < 0.0001$; ns, not significant, 2-way ANOVA).

Figure 5. Bhlhe40 supports glycolysis and oxidative phosphorylation in CD8 T cells in a therapy-dependent manner. (A) Dot plot showing expression of select glycolytic genes (*Aldoa, Gapdh, Eno1,* etc.) in all CD8 T cell clusters. **(B)** GSEA showing enrichment of Hallmark glycolysis pathway in PD1^{hi}_Eff_Ex and Nr4a1^{hi}_Eff_Ex cluster between $B^{f/f}$ vs $B^{\Delta CD8}$ mice with anti-PD-1 treatment. **(C)** XF real-time ATP production rate comparing glycolytic, mitochondrial, and total ATP on *ex vivo* intratumoral CD8 T cells in $B^{f/f}$ and $B^{\Delta CD8}$ mice treated with control Ab, anti-PD-1, or anti-CTLA-4. **(D)** XF real-time ATP Seahorse assay showing ECAR and OCR on *ex vivo* intratumoral CD8 T cells in $B^{f/f}$ and $B^{\Delta CD8}$ mice treated with control Ab, anti-PD-1, or anti-CTLA-4. For statistical comparisons in **(C)**, grey: mitochondrial ATP, blue: glycolytic ATP, and black: total ATP. **(C)** and **(D)** are representative of two independent experiments (∗∗$p < 0.01$; ∗∗∗$p < 0.001$; ns, not significant, unpaired t-test or 2-way ANOVA).

Figure 6. CD4 T cell-intrinsic Bhlhe40 sustains anti-CTLA-4-driven Th1 responses. (A) UMAP generated from integration of CD4 T cells depicting conventional CD4 T cell, Treg, and mixed conventional CD4 T cell and Treg clusters. **(B)** Violin plots showing *Bhlhe40* expression in CD4 T cells by cluster and treatment in $B^{f/f}$ mice. **(C)** Heatmaps comparing features (module scores) of CD4 T cell clusters (rows) to published human CD4 T cell gene signatures (columns) identified/annotated by Chu et al. and Oliveira et al. **(D)** Stacked bar graph showing Th1 clusters as a percentage of CD4 T cells from $B^{f/f}$, $B^{\Delta T}$ and $B^{\Delta CD8}$ mice treated with control Ab, anti-PD-1, or anti-CTLA-4. **(E)** Violin plot showing *Ifng* expression in $ICOS^{hi}Bhlhe40^{hi}$_Th1_6, $ICOS^{+}Bhlhe40^{+}$_Th1_7, and $Gzmk^{+}$_Th1_8 CD4 clusters by treatment in $B^{f/f}$, $B^{\Delta T}$, or $B^{\Delta CD8}$ mice. **(F)** Dot plot displaying select glycolytic transcript expression level and percent of cells in CD4 Th1 clusters.

Figure 7. *BHLHE40* expression correlates with effector and exhaustion-associated programs in human intratumoral CD8 T cells. (**A**) Gene co-expression heatmap of human intratumoral CD8 T cells. (**B**) Feature plot showing expression of *BHLHE40, TOX, TCF7*, and *IFNG* in CD8 T cell clusters (left) from human basal cell carcinoma as identified and annotated by Yost et al., UMAP showing clusters positive or negative for *BHLHE40* and *TCF7* (middle), and dot plot displaying expression of select transcripts in CD8 T cell clusters (right). **(C)** Dot plot of CD8 T cells from pre- and post-treatment with anti-PD-1 basal cell carcinoma patients reveals elevated *BHLHE40* expression in activated and exhausted CD8 T cells. (**D**) Volcano plot showing differential expression of persistent clonotypes between responders and non-responders in pre- and post-treatment in Yost et al. Reanalysis of scRNAseq data from Sade-Feldman et al., Minowa et al., and Yost et al. shown in (**A**). Reanalysis of scRNAseq data from Yost et al shown in **(B-D)**. For **(C)**, $*p < 0.05$; $**p < 0.01$; $***p < 0.001$, Wilcoxon Rank-Sum test. For **(D)**, significantly differentially expressed transcripts ($\log_2FC > 0.5$, adjusted *P* value < 0.05) are

shown in red. Statistical analysis was performed using a two-sided nonparametric Wilcoxon rank sum test with Bonferroni's correction.

SUPPLEMENTARY FIGURE LEGENDS:

Figure S1. Validation of Bhlhe40 deletion and 1956 and Y1.7LI tumor-growth in BΔT and BΔCD8 mice and in CD8 E8I-Cre Bhlhe40+/+ and Bf/f mice under anti-PD-1 or anti-CTLA-4 ICT. (A) Bar graph showing relative Bhlhe40 mRNA expression in CD4 and CD8 T cells isolated from 1956 tumors in Bhlhe40fl/fl (Bf/f) and Bhlhe40ΔCD8 (BΔCD8) mice treated with control antibody (Ab), anti-PD-1, or anti-CTLA-4. **(B)** Tumor growth curve of 1956 tumors in Bf/f and Bhlhe40ΔT (BΔT) mice treated with control antibody (Ab), anti-PD-1, or anti-CTLA-4. **(C)** Bhlhe40 conditional knockout mice bearing Y1.7LI melanoma tumors were treated with anti-PD-1 or anti-CTLA-4 as indicated. **(D)** Tumor growth and percent tumor rejection of Y1.7LI melanoma tumors in Bf/f and BΔCD8 mice treated with control Ab, anti-PD-1, or anti-CTLA-4. **(E)** Tumor growth curve of 1956 tumors between CD8 E8I-Cre Bhlhe40+/+ mice and Bf/f mice treated with control Ab, anti-PD-1, or anti-CTLA-4. For (A), RNA was isolated from intratumoral CD4 and CD8 T cells sorted from 1956 tumors in Bf/f and BΔCD8 treated with control Ab, anti-PD-1, or anti-CTLA-4. Bar graphs display the mean ± SEM and are representative of at least three independent experiments (*$p<0.05$, ∗∗$p < 0.01$; ns, not significant, unpaired t test). For **(B)** and **(D)**, tumor growth is presented as mean +/- SEM of mean tumor diameter of mice. Tumor rejection graphs display cumulative percentage of mice with complete tumor rejection and are representative of at least three independent experiments (∗∗∗$p < 0.001$; ∗∗∗∗$p < 0.0001$; ns, not significant, 2-way ANOVA).

Figure S2. Single cell RNAseq integration and analysis of intratumoral CD8 T cells from Bf/f, BΔT, and BΔCD8 mice treated with anti-PD-1 or anti-CTLA-4 ICT. (A) Schematic of

experimental design for peptide-MHC (pMHC) tetramer staining and for scRNAseq Experiment #1 (scRNA_1) and Experiment #2 (scRNA_2). **(B)** Workflow to generate integrated scRNAseq datasets. **(C)** Violin plots denoting expression levels of select genes in each CD8 clusters. **(D)** Dot plot showing the regulon specificity score across transcription factors. The top five regulons and Bhlhe40 in Nr4a1hi_Eff/Ex, Toxhi_Eff/Ex and Naïve_Mem cluster are highlighted in red and labeled on the plot. **(E)** Stacked bar graph showing clusters as a percentage of total CD8 T cells from Bf/f, B□T and BΔCD8 mice under different treatment conditions. **(F)** Scatter plot displaying Tcf7 and Tox expression in cells within Toxhi_Eff_Ex cluster and 2x2 contingency table showing number of cells within Toxhi_Eff_Ex expressing Tcf7 and/or Tox.

Figure S3. Heat map displaying normalized expression of select genes by CD8 T cell cluster and condition.

Figure S4. Select gene expression profiles of CD8 T cell clusters from integrated scRNAseq analysis. (A) Dot plot displaying expression level and percent of cells expressing select genes in CD8 T cell clusters. **(B)** Dot plot showing Il-10 expression in clusters PD1hi_Eff_Ex and Nr4a1hi_Eff_Ex. **(C)** Dot plot showing expression level and percent of cells expressing Tox by treatment condition in Bf/f vs BΔCD8 mice in all CD8 clusters.

Figure S5. GSEA in PD1hi_Eff_Ex, Nr4a1hi_Eff_Ex, Toxhi_Eff_Ex, Cd39+_Eff_Ex, Naïve_memory, and Tpexlike_Ifn-stim CD8 clusters with anti-PD-1 treatment between Bf/f and BΔCD8 mice. White indicates non-significant hallmark pathways; red indicates significantly upregulated hallmark pathways; blue indicates significantly downregulated hallmark pathways).

Figure S6. GSEA in CD8 Tcell clusters with anti-CTLA-4 treatment between Bf/f and BΔCD8 mice. White indicates non-significant hallmark pathways; red indicates significantly upregulated hallmark pathways; blue indicates significantly downregulated hallmark pathways.

Figure S7. (A) Bar plot showing Spearman correlation of all genes with Bhlhe40 in the CD8 T cell clusters in Bf/f mice. Orange dots indicate genes are positively correlated to Bhlhe40, blue dots indicate negative correlation. Metabolic transcripts are indicated in purple dots. **(B)** Gene-concept network showing Reactome pathway enrichment based on the top 50 genes most strongly correlated with Bhlhe40. Yellow dots represent pathways; grey dots represent gene name. Connecting lines indicate that a given gene is part of the corresponding pathway.

Figure S8. Tcf7 expression in CD8 T cell clusters and reduced tumor control by Bhlhe40-deficient OT-1 T cells in the B16-OVA model (A) Tcf7 feature plot of CD8 T cell clusters. **(B)** Dot plot showing expression level and percent of cells expressing Tcf7 and Bach2 by treatment condition in Bf/f vs BΔCD8 mice in all CD8 clusters, Naïve_Mem, Tpexlike_Ifn-stim, and Toxhi Eff_Ex clusters. **(C)** Feature plot showing expression of BHLHE40, TOX, TCF7, and IFNG in CD8 T cell clusters from human triple-negative breast cancer (TNBC) as identified and annotated by Bassez et al. **(D)** Dot plot displaying expression of select transcripts in CD8 T cell clusters. **(C-D)** Reanalysis of scRNAseq data of CD8 T cells from TNBC from Bassez et al.

Figure S9. Differentially expressed genes and metabolic gene expression in effector/exhausted CD8 T cell clusters following Bhlhe40 deletion. (A) Volcano plot showing differentially expressed genes between Bf/f and BΔCD8 mice treated with anti-PD-1 in PD1hi_Eff_Ex, Nr4a1hi_Eff_Ex and Toxhi_Eff_Ex clusters. Significantly differentially expressed transcripts (log2FC < −0.5 or log2FC > 0.5, adjusted P value < 0.05) are shown in red. Statistical analysis was performed using a two-sided nonparametric Wilcoxon rank sum test with

Bonferroni's correction. **(B)** Dot plot displaying expression level and percent of cells expressing select glycolytic transcripts in effector/exhausted CD8 T cell clusters. **(C)** Dot plot displaying expression level and percent of cells expressing select OXPHOS transcripts in effector/exhausted CD8 T cell clusters.

Figure S10. CD4 T cell subset composition and transcriptional profiles under ICT in Bf/f, B□T and BΔCD8 mice. (A) Bar graph showing percent of conventional CD4 T cells and Foxp3+ Tregs from Bf/f and BΔCD8 mice treated with control Ab, anti-PD-1, or anti-CTLA-4. Bar graphs display the mean ± SEM and are representative of at least three independent experiments (*p<0.05, unpaired t test). **(B)** Stacked bar graph showing fraction of the subtypes of CD4 T cells and Tregs. **(C)** Dot plot showing expression level and percent of cells in select genes in ICOShiBhlhe40hi_Th1_6, ICOS+Bhlhe40+_Th1_7, and Gzmk+_Th1_8 CD4 T cell clusters. **(D)** Heat map displaying normalized expression of select genes in each CD4 T cell clusters by treatment condition in Bf/f, BΔCD8, and BΔT mice.

Figure S11. Bhlhe40-dependent T cell mediated macrophage remodeling following ICT. (A) UMAP generated from scRNAseq Experiment 1 (scRNA_1) by subclustering only macrophage clusters from Bf/f, BΔT, or BΔCD8 mice. **(B)** Heat map displaying average expression of select genes in monocyte/macrophage by clusters. **(C)** Dot plot showing expression level and percent of cells expressing select genes in all macrophage clusters between Bf/f, BΔT, or BΔCD8 mice. **(D)** Stacked bar graph showing clusters as a percentage of total macrophage from Bf/f, BΔT and BΔCD8 mice treated with control Ab, anti-PD-1, or anti-CTLA-4. **(E)** Representative flow cytometry plots (gated on macrophages) displaying intratumoral CX3CR1+CD206+ and iNOS+ macrophages from 1956 tumor bearing Bf/f, BΔT, or BΔCD8 mice treated with control Ab, anti-PD-1 or anti-CTLA-4 and harvested on day 10 post-tumor transplant and are representative of at least three independent experiments.

gure 1

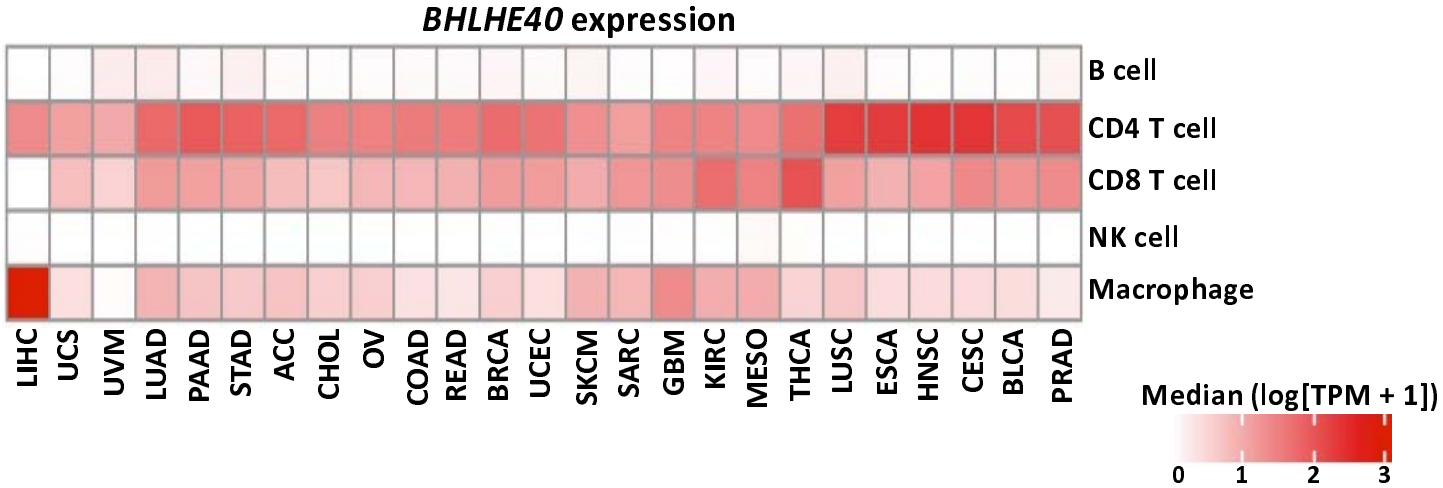
BHLHE40 expression
B cell
CD4 T cell
CD8 T cell
NK cell
Macrophage
LIHC
UCS
UVM
LUAD
PAAD
STAD
ACC
CHOL
OV
COAD
READ
BRCA
UCEC
SKCM
SARC
GBM
KIRC
MESO
THCA
LUSC
ESCA
HNSC
CESC
BLCA
PRAD
Median (log[TPM + 1])
0
1
2
3

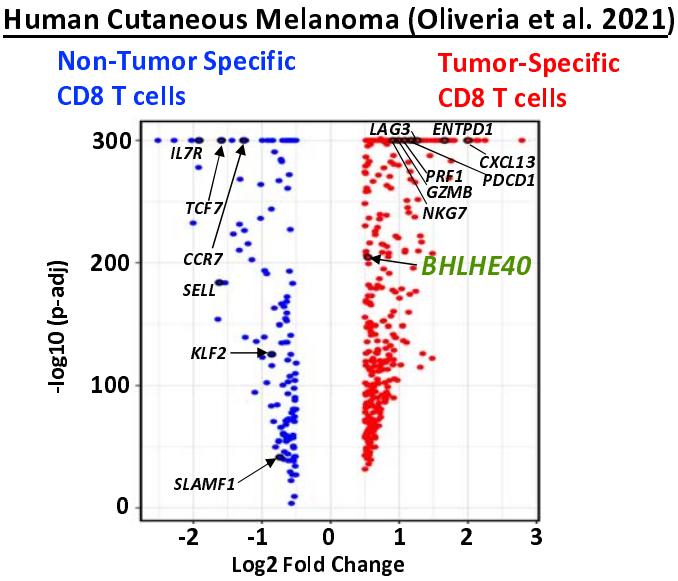
Human Cutaneous Melanoma (Oliveria et al. 2021)
Non-Tumor Specific
CD8 T cells
Tumor-Specific
CD8 T cells
IL7R
TCF7
CCR7
SELL
KLF2
SLAMF1
LAG3
ENTPD1
CXCL13
PDCD1
PRF1
GZMB
NKG7
BHLHE40
-log10 (p-adj)
Log2 Fold Change

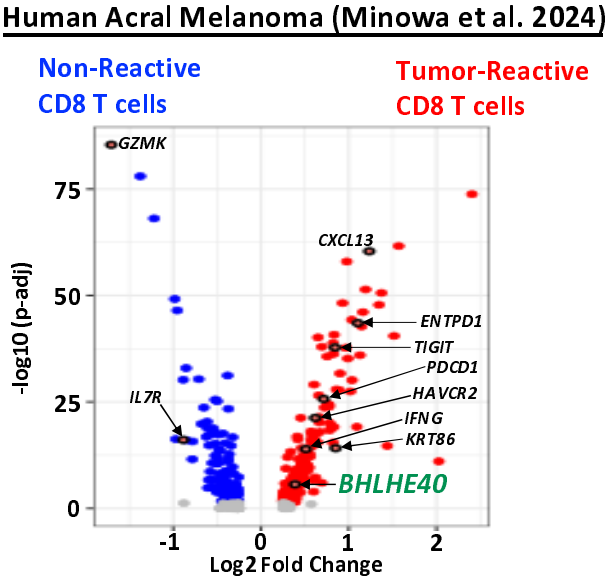
Human Acral Melanoma (Minowa et al. 2024)
Non-Reactive
CD8 T cells
Tumor-Reactive
CD8 T cells
GZMK
IL7R
CXCL13
ENTPD1
TIGIT
PDCD1
HAVCR2
IFNG
KRT86
BHLHE40
-log10 (p-adj)
Log2 Fold Change

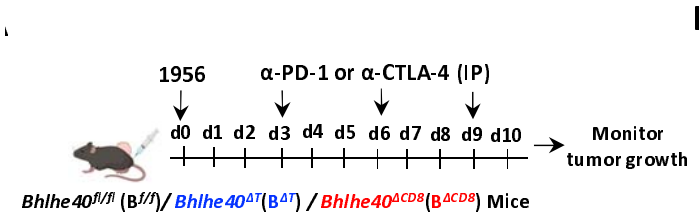
1956
α-PD-1 or α-CTLA-4 (IP)
d0 d1 d2 d3 d4 d5 d6 d7 d8 d9 d10
Monitor tumor growth
Bhlhe40fl/fl (Bf/f)/ Bhlhe40ΔT(BΔT) / Bhlhe40ΔCD8(BΔCD8) Mice

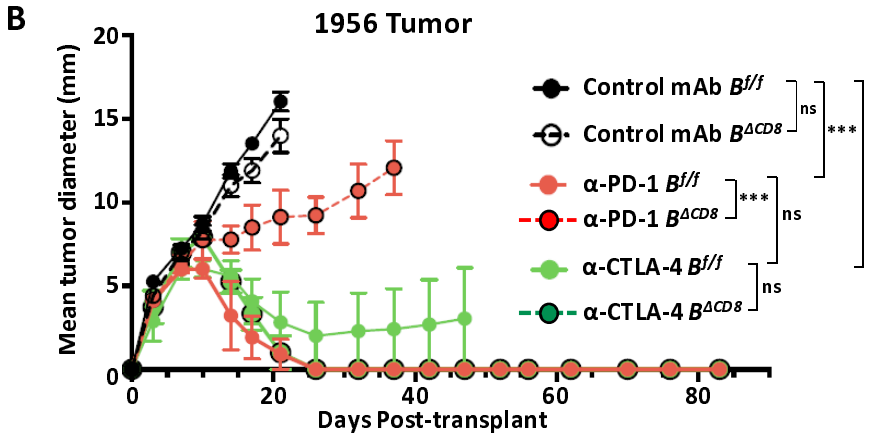
B
1956 Tumor
Mean tumor diameter (mm)
Days Post-transplant
Control mAb Bf/f
Control mAb BΔCD8
α-PD-1 Bf/f
α-PD-1 BΔCD8
α-CTLA-4 Bf/f
α-CTLA-4 BΔCD8
ns
***

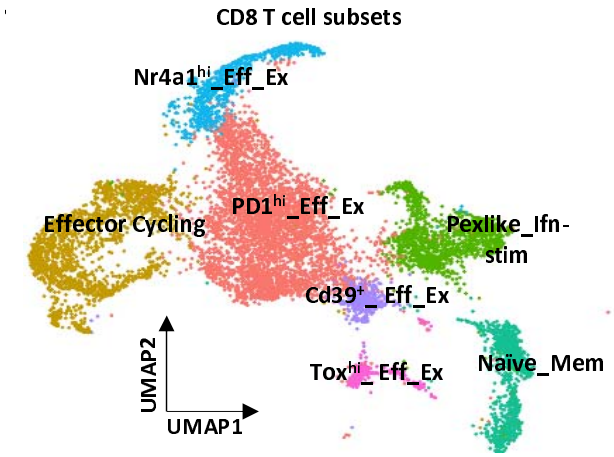
CD8 T cell subsets
Nr4a1hi_Eff_Ex
PD1hi_Eff_Ex
Effector Cycling
Pexlike_Ifn-stim
Cd39+_Eff_Ex
Toxhi_Eff_Ex
Naïve_Mem
UMAP2
UMAP1

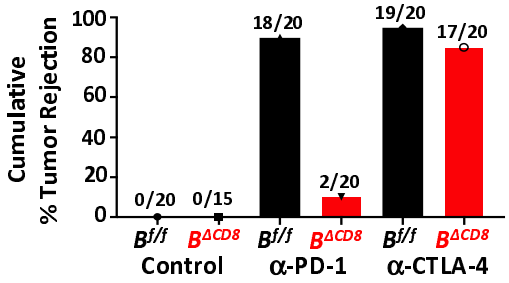
Cumulative % Tumor Rejection
0/20
0/15
18/20
2/20
19/20
17/20
Bf/f
BΔCD8
Control
α-PD-1
α-CTLA-4

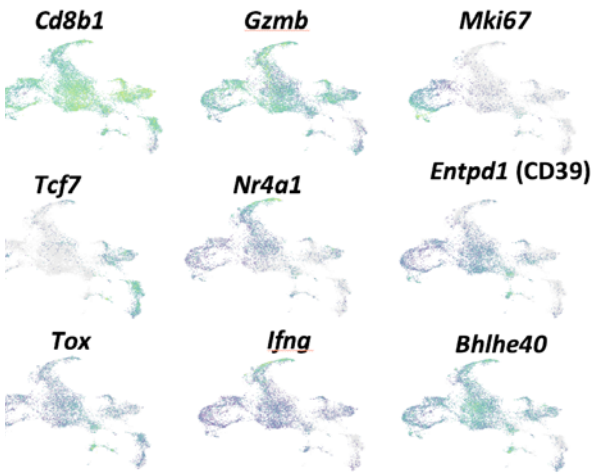
Cd8b1
Gzmb
Mki67
Tcf7
Nr4a1
Entpd1 (CD39)
Tox
Ifng
Bhlhe40

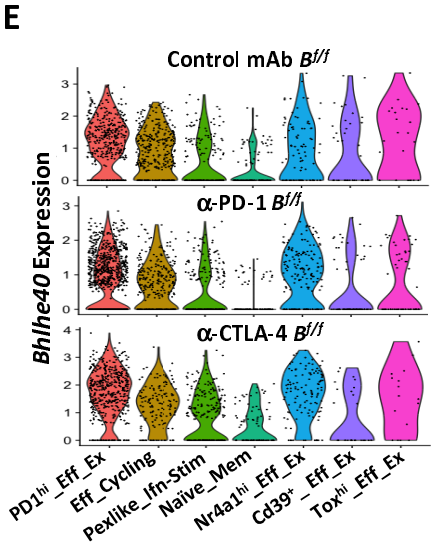
E
Control mAb Bf/f
α-PD-1 Bf/f
α-CTLA-4 Bf/f
Bhlhe40 Expression
PD1hi_Eff_Ex
Eff_Cycling
Pexlike_Ifn-Stim
Naïve_Mem
Nr4a1hi_Eff_Ex
Cd39+_Eff_Ex
Toxhi_Eff_Ex

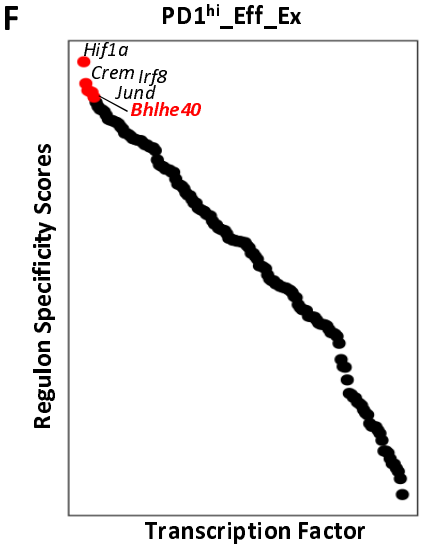
F
PD1hi_Eff_Ex
Hif1a
Crem
Irf8
Jund
Bhlhe40
Regulon Specificity Scores
Transcription Factor

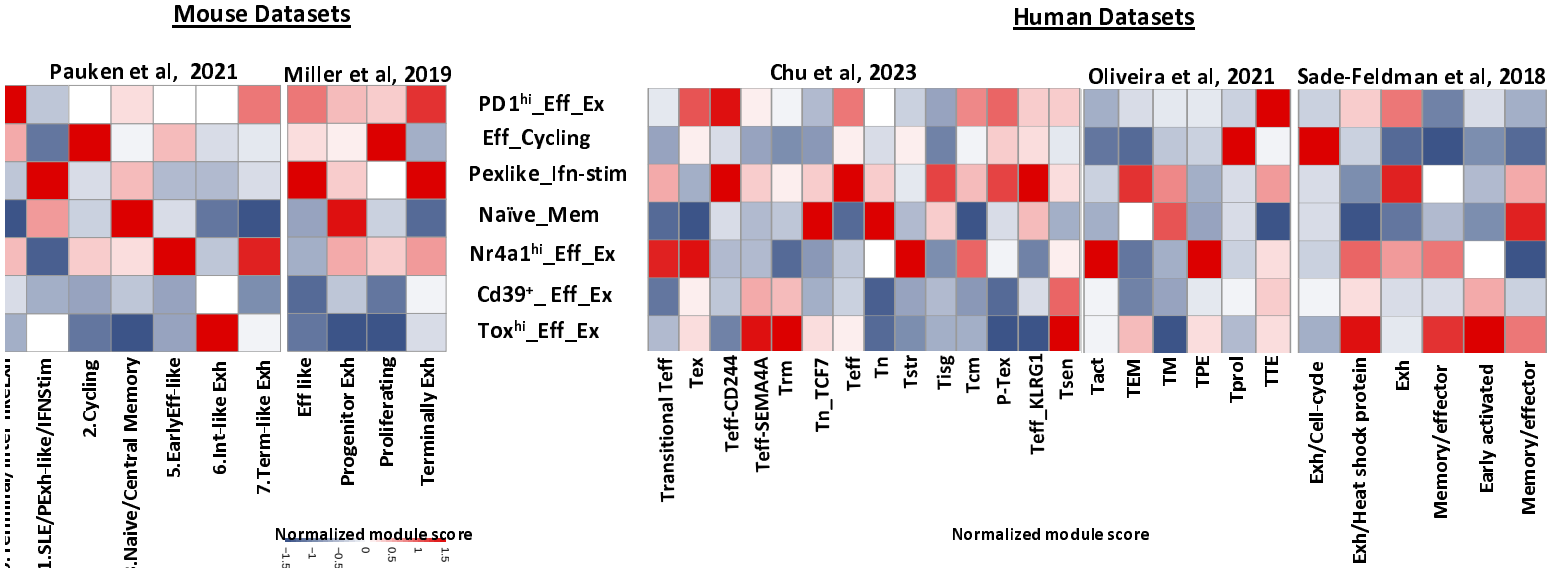
Mouse Datasets
Human Datasets
Pauken et al, 2021
Miller et al, 2019
Chu et al, 2023
Oliveira et al, 2021
Sade-Feldman et al, 2018
PD1hi_Eff_Ex
Eff_Cycling
Pexlike_Ifn-stim
Naïve_Mem
Nr4a1hi_Eff_Ex
Cd39+_ Eff_Ex
Toxhi_Eff_Ex
1.SLE/PExh-like/IFNStim
2.Cycling
5.EarlyEff-like
6.Int-like Exh
7.Term-like Exh
Eff like
Progenitor Exh
Proliferating
Terminally Exh
Transitional Teff
Tex
Teff-CD244
Teff-SEMA4A
Trm
Tn_TCF7
Teff
Tn
Tstr
Tisg
Tcm
P-Tex
Teff_KLRG1
Tsen
Tact
TEM
TM
TPE
Tprol
TTE
Exh/Cell-cyde
Exh/Heat shock protein
Exh
Memory/effector
Early activated
Memory/effector
Normalized module score

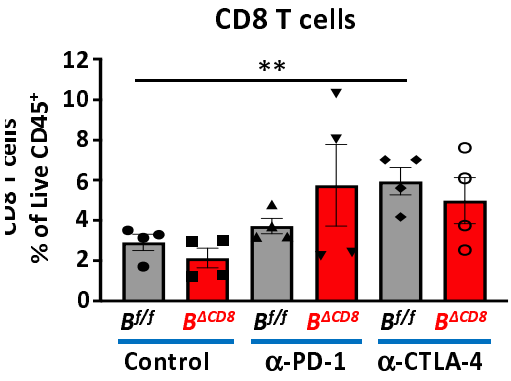
CD8 T cells
% of Live CD45+
**
Bf/f
BΔCD8
Control
α-PD-1
α-CTLA-4

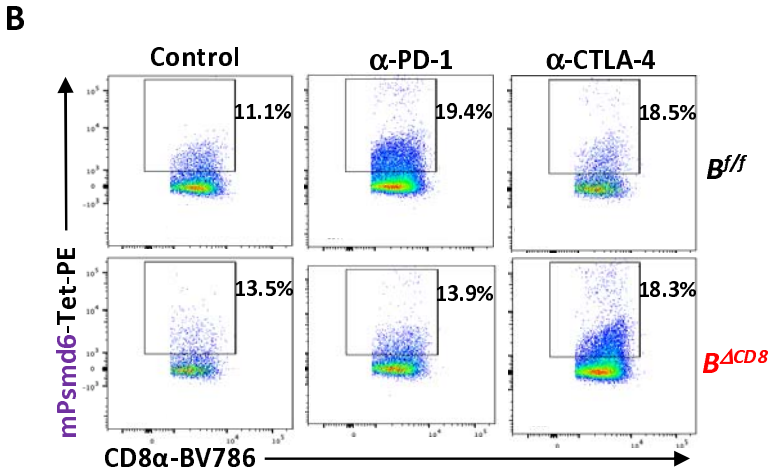
B
Control
α-PD-1
α-CTLA-4
11.1%
19.4%
18.5%
13.5%
13.9%
18.3%
Bf/f
BΔCD8
mPsmd6-Tet-PE
CD8α-BV786

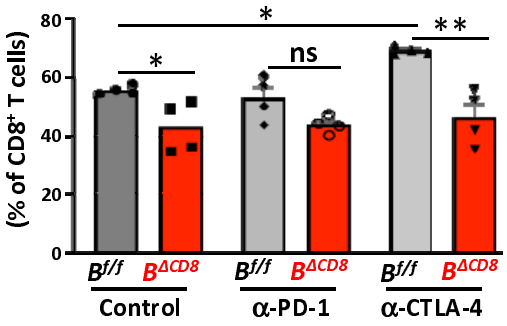
(% of CD8+ T cells)
*
ns
**
Bf/f
BΔCD8
Control
α-PD-1
α-CTLA-4

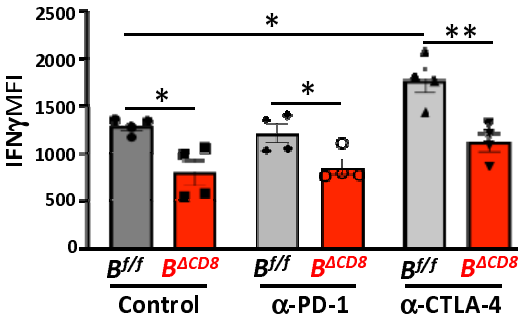
IFNγMFI
*
**
Bf/f
BΔCD8
Control
α-PD-1
α-CTLA-4

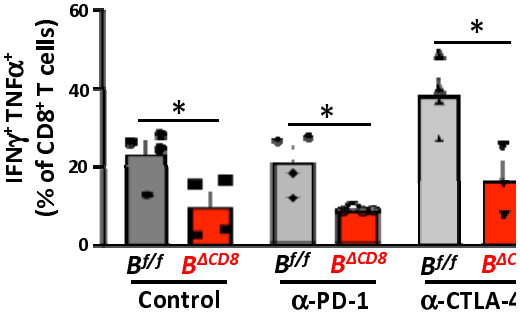
IFNγ+TNFα+
(% of CD8+ T cells)
*
Bf/f
BΔCD8
Control
α-PD-1

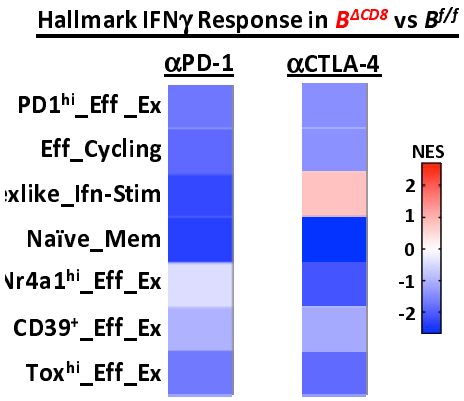
Hallmark IFNγ Response in BΔCD8 vs Bf/f
αPD-1
αCTLA-4
PD1hi_Eff _Ex
Eff_Cycling
xlike_Ifn-Stim
Naïve_Mem
Nr4a1hi_Eff_Ex
CD39+_Eff_Ex
Toxhi_Eff_Ex
NES

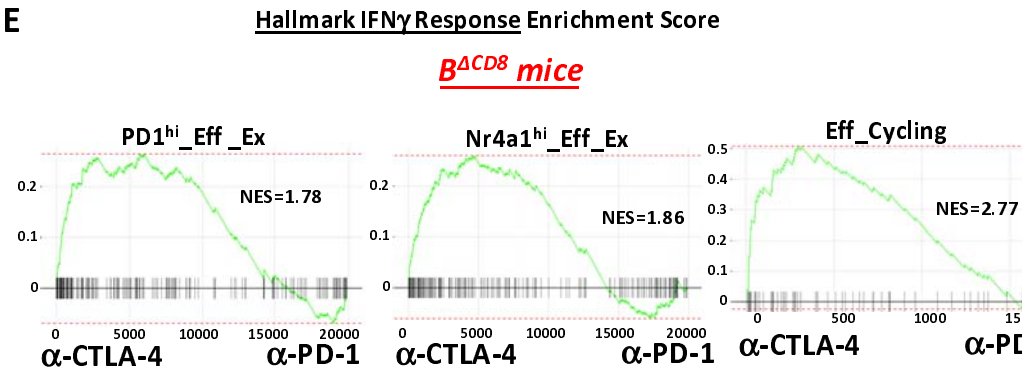
E
Hallmark IFNγ Response Enrichment Score
BΔCD8 mice
PD1hi_Eff _Ex
NES=1.78
Nr4a1hi_Eff_Ex
NES=1.86
Eff_Cycling
NES=2.77
α-CTLA-4
α-PD-1

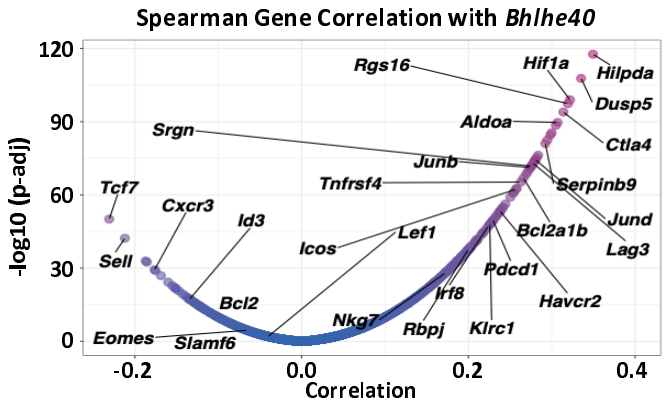
Spearman Gene Correlation with Bhlhe40
-log10 (p-adj)
Correlation
Rgs16
Hif1a
Hilpda
Dusp5
Aldoa
Ctla4
Srgn
Junb
Tnfrsf4
Serpinb9
Tcf7
Cxcr3
Id3
Jund
Lef1
Bcl2a1b
Lag3
Icos
Sell
Pdcd1
Irf8
Havcr2
Bcl2
Nkg7
Rbpj
Klrc1
Eomes
Slamf6

B

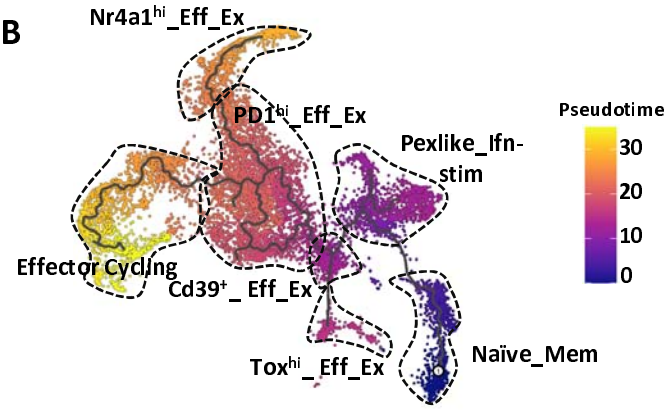
Nr4a1hi_Eff_Ex
PD1hi_Eff_Ex
Pexlike_Ifn-stim
Pseudotime
Effector Cycling
Cd39+_Eff_Ex
Naïve_Mem
Toxhi_Eff_Ex

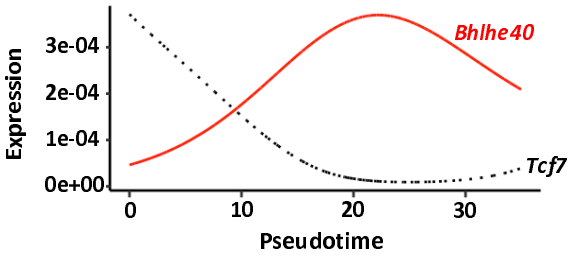
Expression
Bhlhe40
Tcf7
Pseudotime

D

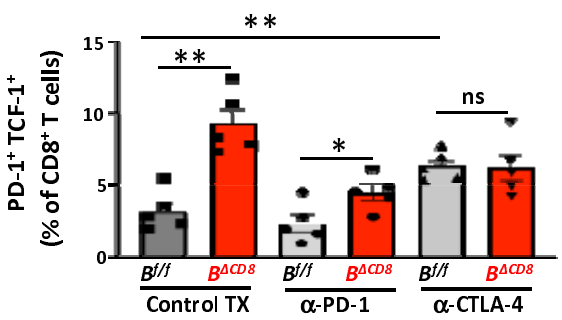
PD-1+ TCF-1+ (% of CD8+ T cells)
Control TX
α-PD-1
α-CTLA-4
ns

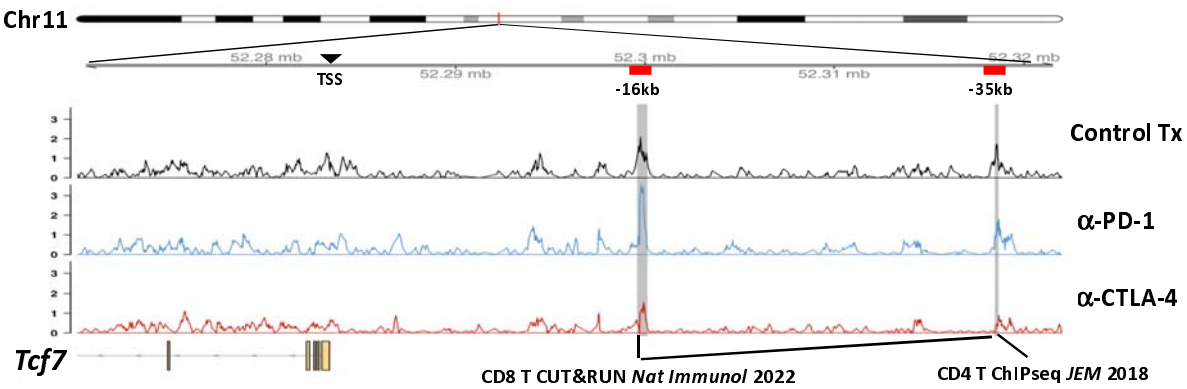
Chr11
TSS
-16kb
-35kb
Control Tx
α-PD-1
α-CTLA-4
Tcf7
CD8 T CUT&RUN Nat Immunol 2022
CD4 T ChIPseq JEM 2018

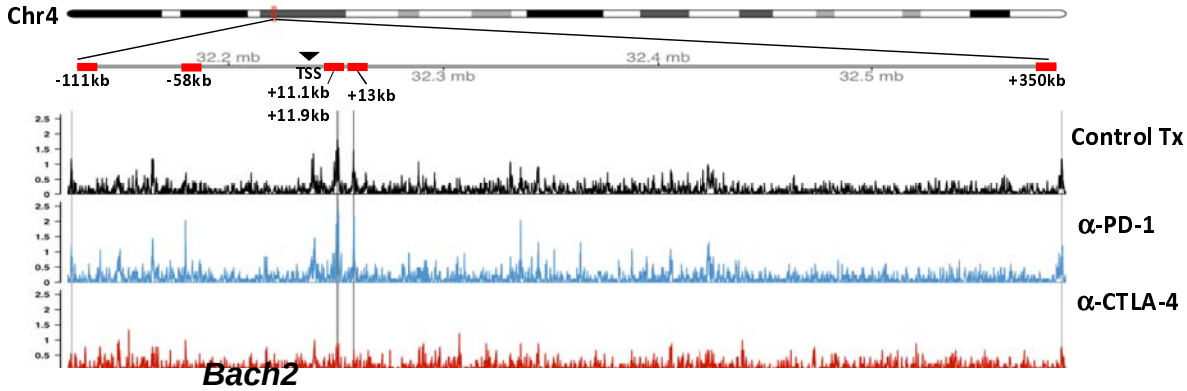
Chr4
-111kb
-58kb
TSS
+11.1kb
+11.9kb
+13kb
+350kb
Control Tx
α-PD-1
α-CTLA-4
Bach2

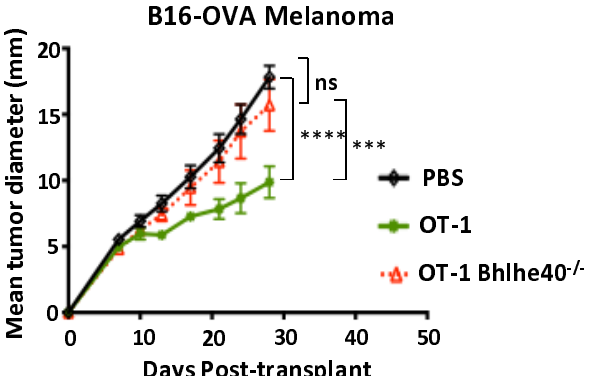
B16-OVA Melanoma
Mean tumor diameter (mm)
Days Post-transplant
ns
****
***
PBS
OT-1
OT-1 Bhlhe40-/-

H

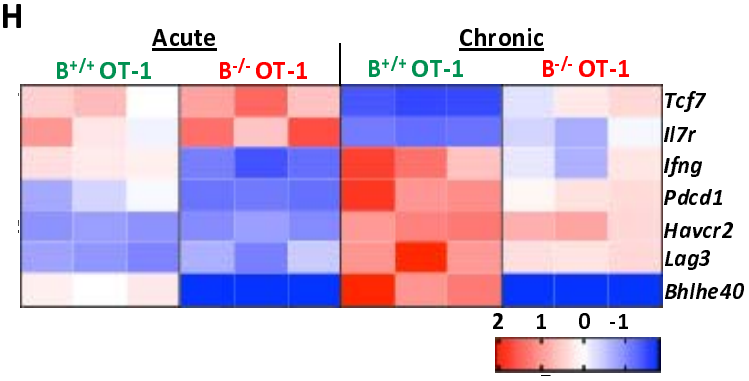
Acute
Chronic
B+/+ OT-1
B-/- OT-1
B+/+ OT-1
B-/- OT-1
Tcf7
Il7r
Ifng
Pdcd1
Havcr2
Lag3
Bhlhe40

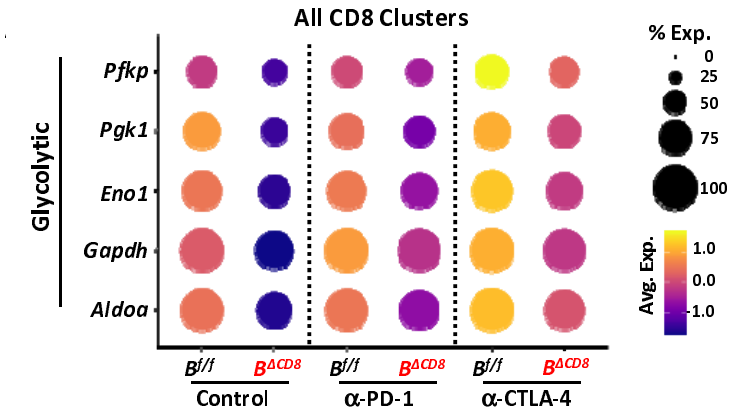
All CD8 Clusters
Glycolytic
Pfkp
Pgk1
Eno1
Gapdh
Aldoa
% Exp.
0
25
50
75
100
Avg. Exp.
1.0
0.0
-1.0
Bf/f
BΔCD8
Control
α-PD-1
α-CTLA-4

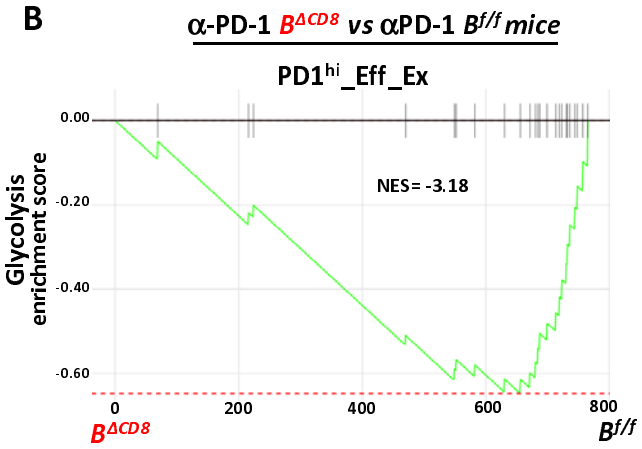
B
α-PD-1 BΔCD8 vs αPD-1 Bf/f mice
PD1hi_Eff_Ex
Glycolysis enrichment score
NES= -3.18
0.00
-0.20
-0.40
-0.60
0
200
400
600
800
BΔCD8
Bf/f

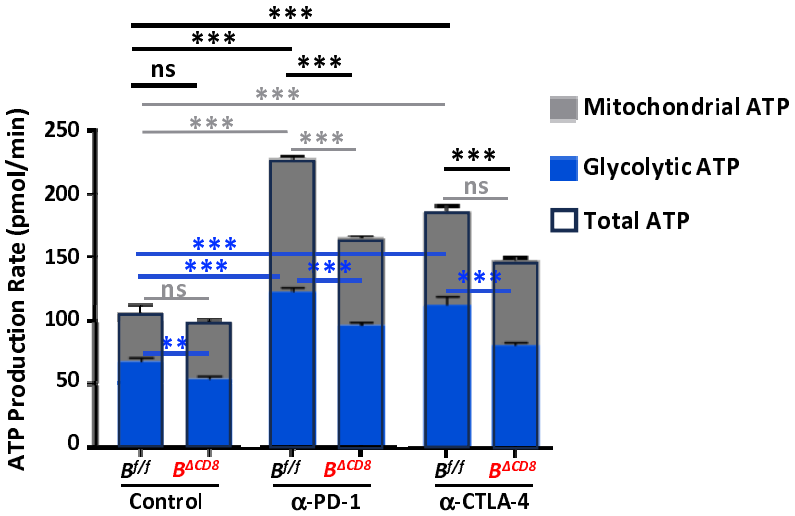
ATP Production Rate (pmol/min)
250
200
150
100
50
0
Mitochondrial ATP
Glycolytic ATP
Total ATP
***
ns
Bf/f
BΔCD8
Control
α-PD-1
α-CTLA-4

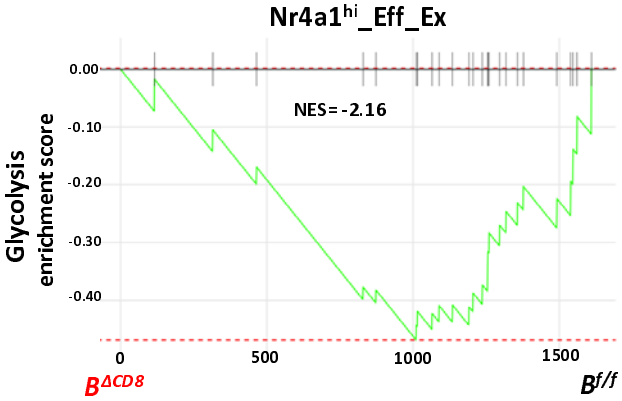
Nr4a1hi_Eff_Ex
Glycolysis enrichment score
NES= -2.16
0.00
-0.10
-0.20
-0.30
-0.40
0
500
1000
1500
BΔCD8
Bf/f

ECAR

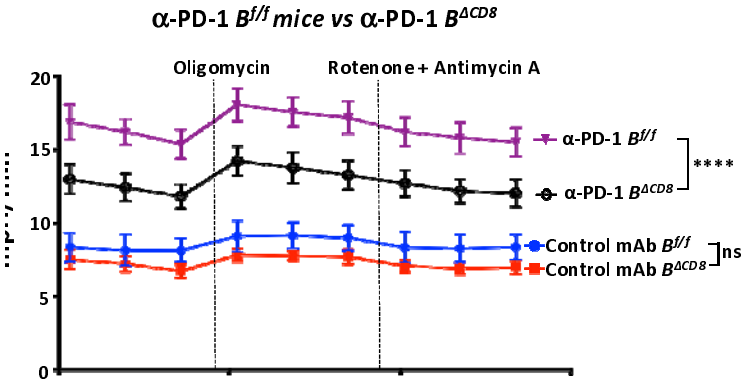
α-PD-1 Bf/f mice vs α-PD-1 BΔCD8
Oligomycin
Rotenone + Antimycin A
α-PD-1 Bf/f
α-PD-1 BΔCD8
Control mAb Bf/f
Control mAb BΔCD8
****
ns
20
15
10
5
0

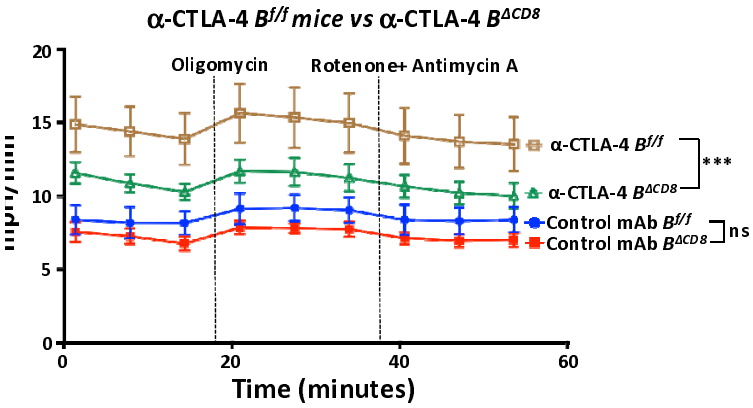
α-CTLA-4 Bf/f mice vs α-CTLA-4 BΔCD8
Oligomycin
Rotenone+ Antimycin A
α-CTLA-4 Bf/f
α-CTLA-4 BΔCD8
Control mAb Bf/f
Control mAb BΔCD8
***
ns
20
15
10
5
0
0
20
40
60
Time (minutes)

OCR

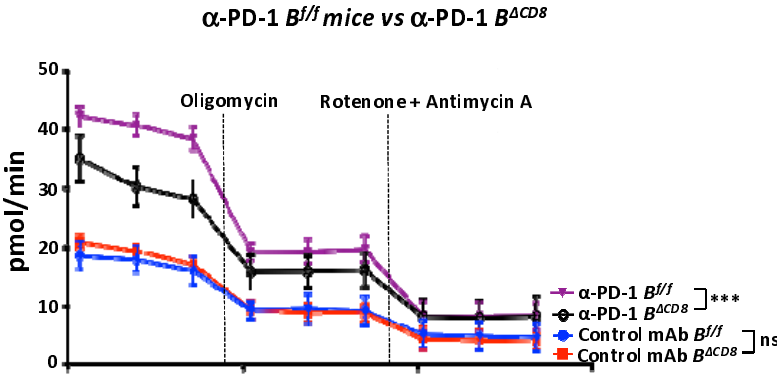
α-PD-1 Bf/f mice vs α-PD-1 BΔCD8
Oligomycin
Rotenone + Antimycin A
pmol/min
50
40
30
20
10
0
α-PD-1 Bf/f
α-PD-1 BΔCD8
Control mAb Bf/f
Control mAb BΔCD8
***
ns

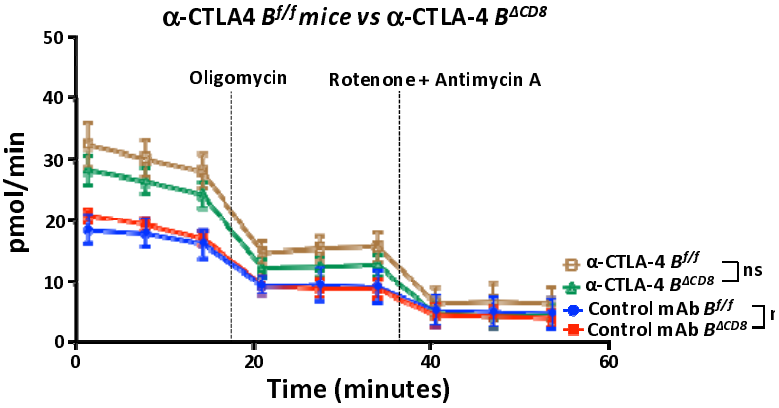
α-CTLA4 Bf/f mice vs α-CTLA-4 BΔCD8
Oligomycin
Rotenone + Antimycin A
pmol/min
50
40
30
20
10
0
α-CTLA-4 Bf/f
α-CTLA-4 BΔCD8
Control mAb Bf/f
Control mAb BΔCD8
ns
0
20
40
60
Time (minutes)

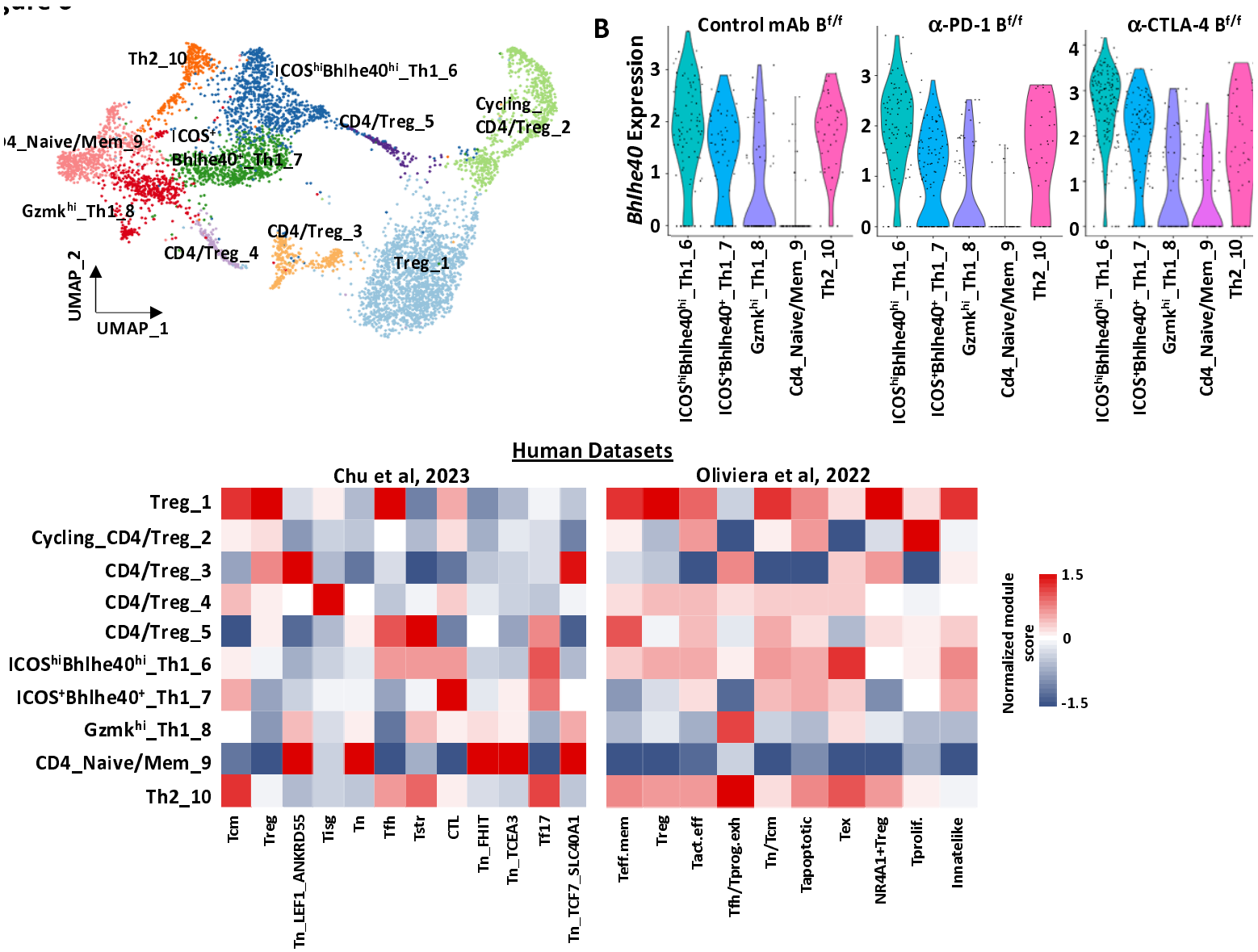
Th2_10
ICOS^hiBhlhe40^hi_Th1_6
Cycling_CD4/Treg_2
CD4/Treg_5
ICOS+Bhlhe40+_Th1_7
Gzmk^hi_Th1_8
CD4/Treg_3
CD4/Treg_4
Treg_1
UMAP_2
UMAP_1
B
Control mAb B^f/f
α-PD-1 B^f/f
α-CTLA-4 B^f/f
Bhlhe40 Expression
ICOS^hiBhlhe40^hi_Th1_6
ICOS+Bhlhe40+_Th1_7
Gzmk^hi_Th1_8
Cd4_Naive/Mem_9
Th2_10
Human Datasets
Chu et al, 2023
Oliviera et al, 2022
Treg_1
Cycling_CD4/Treg_2
CD4/Treg_3
CD4/Treg_4
CD4/Treg_5
ICOS^hiBhlhe40^hi_Th1_6
ICOS+Bhlhe40+_Th1_7
Gzmk^hi_Th1_8
CD4_Naive/Mem_9
Th2_10
Tcm
Treg
Tn_LEF1_ANKRD55
Tisg
Tn
Tfh
Tstr
CTL
Tn_FHIT
Tn_TCEA3
Tf17
Tn_TCF7_SLC40A1
Teff.mem
Treg
Tact.eff
Tfh/Tprog.exh
Tn/Tcm
Tapoptotic
Tex
NR4A1+Treg
Tprolif.
Innatelike
Normalized module score
1.5
0
-1.5
ICOS^hiBhlhe40^hi_Th1_6
ICOS+Bhlhe40+_Th1_7
Gzmk^hi_Th1_8
B^f/f
B^ΔCD8
B^ΔT
Control
α-PD-1
α-CTLA-4
E
Ifng Expression level
ICOS^hiBhlhe40^hi_Th1_6
ICOS+Bhlhe40+_Th1_7
Gzmk+_Th1_8
α-CTLA-4
ICOS^hiBhlhe40^hi_Th1_6
ICOS+Bhlhe40+_Th1_7
Gzmk^hi_Th1_8
% Exp.
Avg. Exp.
Control
α-PD-1
α-CTLA-4

gure 7

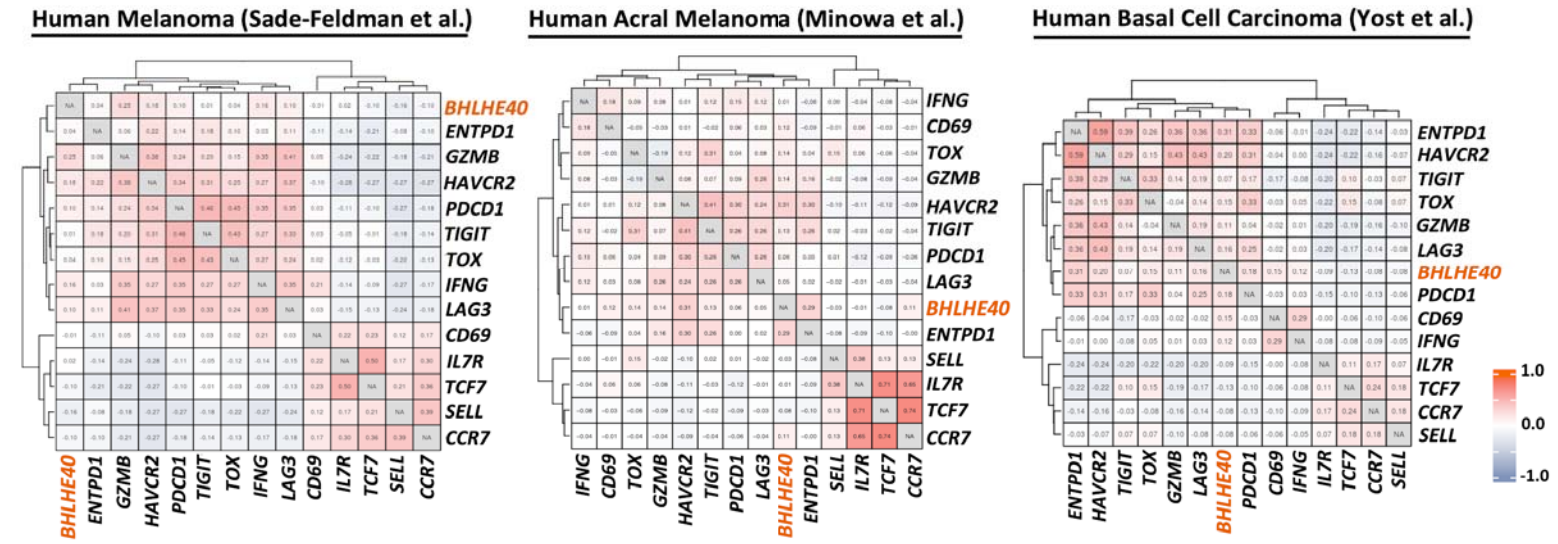
Human Melanoma (Sade-Feldman et al.)
Human Acral Melanoma (Minowa et al.)
Human Basal Cell Carcinoma (Yost et al.)
BHLHE40
ENTPD1
GZMB
HAVCR2
PDCD1
TIGIT
TOX
IFNG
LAG3
CD69
IL7R
TCF7
SELL
CCR7
1.0
0.0
-1.0

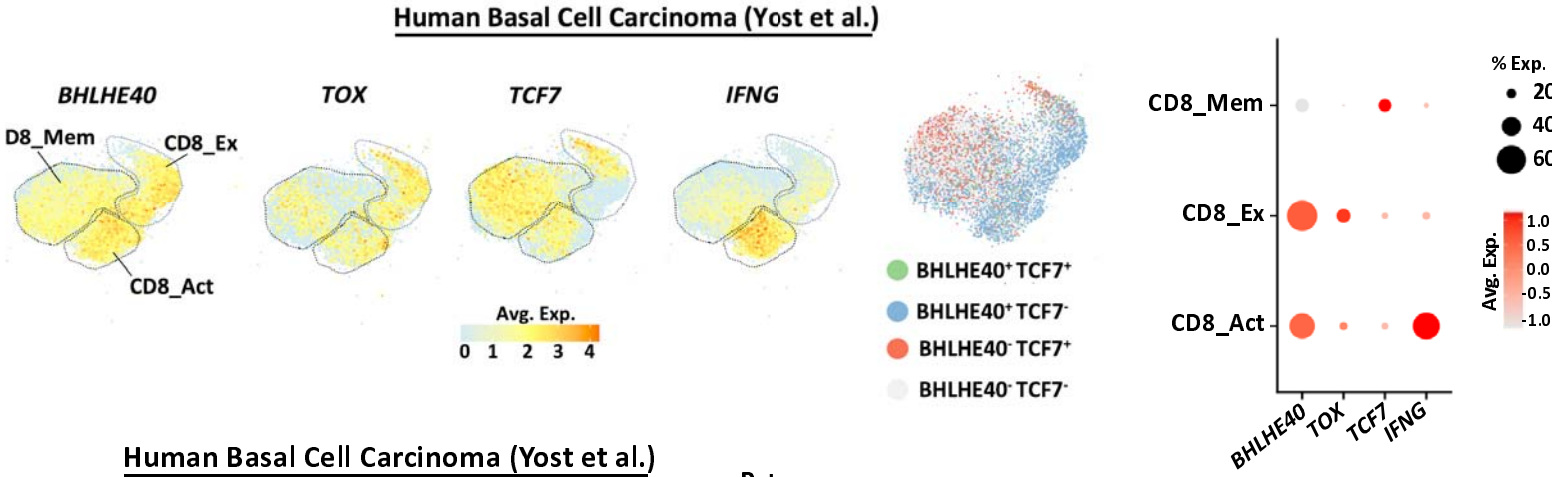
Human Basal Cell Carcinoma (Yost et al.)
BHLHE40
TOX
TCF7
IFNG
D8_Mem
CD8_Ex
CD8_Act
Avg. Exp.
0 1 2 3 4
BHLHE40+ TCF7+
BHLHE40+ TCF7-
BHLHE40- TCF7+
BHLHE40- TCF7-
% Exp.
20
40
60
Avg. Exp.
1.0
0.5
0.0
-0.5
-1.0

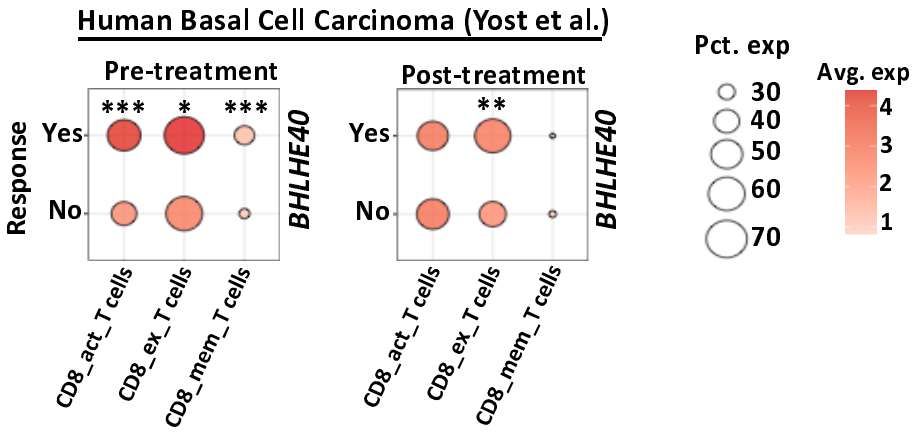
Human Basal Cell Carcinoma (Yost et al.)
Pre-treatment
Post-treatment
Response
Yes
No
BHLHE40
CD8_act_T cells
CD8_ex_T cells
CD8_mem_T cells
Pct. exp
30
40
50
60
70
Avg. exp
4
3
2
1

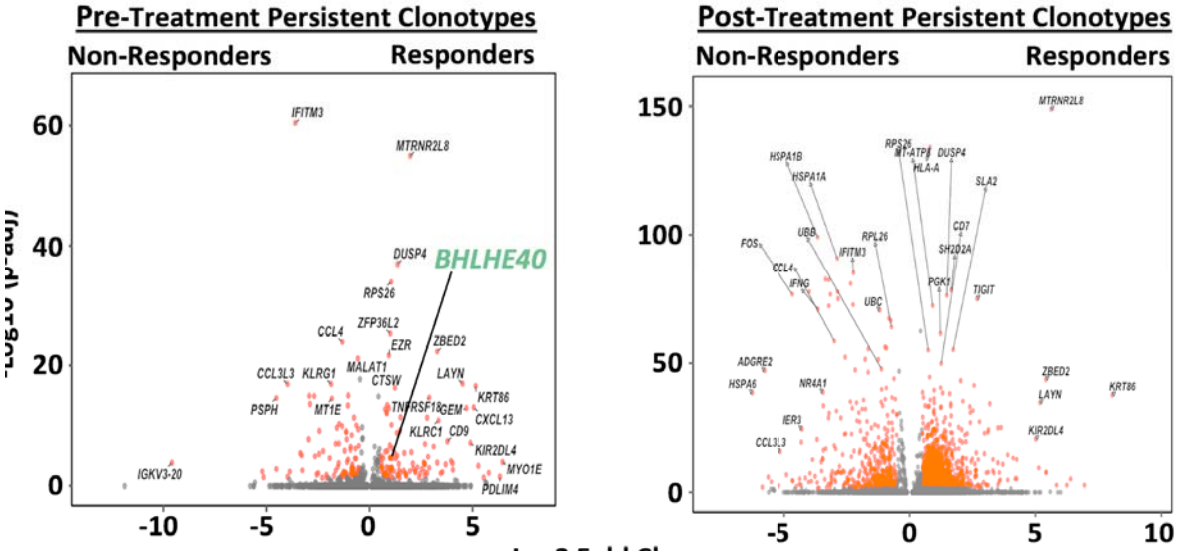
Pre-Treatment Persistent Clonotypes
Non-Responders
Responders
BHLHE40
Post-Treatment Persistent Clonotypes
Non-Responders
Responders